Journal of Asian Earth Sciences 264 (2024) 106040

Contents lists available at ScienceDirect

Journal of Asian Earth Sciences

journal homepage: www.elsevier.com/locate/jseaes

Full length article

Source characterization of Intermediate-Depth earthquakes in southern Java, Indonesia

M. Megawati [a,c,*], Kuo-Fong Ma [a,b,c,d], Po-Fei Chen [c], Dimas Sianipar [e], Ming-Che Hsieh [d]

[a] Taiwan International Graduate Program (TIGP) Earth System Science, Academia Sinica and National Central University, Taipei, Taiwan
[b] Institute of Earth Sciences, Academia Sinica, Taipei, Taiwan
[c] Department of Earth Sciences, National Central University, Taoyuan, Taiwan
[d] Earthquake-Disaster and Risk Evaluation and Management Center (E-DREaM), National Central University, Taoyuan, Taiwan
[e] State College of Meteorology, Climatology, and Geophysics of the Republic of Indonesia (STMKG), Jakarta, Indonesia

ARTICLE INFO

Keywords:
Finite-fault
Rupture process
Source time functions
Intermediate-depth earthquakes
Directivity

ABSTRACT

The rupture behavior of intermediate-depth earthquakes in southern Java remains poorly understood despite their potential seismic hazard. In this study, we performed finite-fault inversions to investigate the rupture processes and source characteristics of five intermediate-depth earthquakes (60–300 km depth) with moment magnitudes (M_W) $\geq$ 6.1 from 1998 to 2017 in the southern region of Java and its surrounding areas. Utilizing teleseismic body waves and surface waves, we employed a wavelet-based seismic inversion technique. Initially, we conducted preliminary inversions of the focal mechanisms (strike and dip) from the Global Centroid Moment Tensor (GCMT) database to determine the optimal fault plane orientation for slip distributions and source time functions (STFs). Our findings reveal that most of the earthquakes exhibited a simple rupture process characterized by a single and compact asperity with a single triangular STF, except for the 1998 earthquake. The results indicate that the ruptures primarily propagated unilaterally along the down-dip direction, except for the 2014 earthquake. We further analyzed the data incorporating directivity, which confirmed the rupture behavior. Three events suggested that the preferred rupture planes were near-vertical (down-dip), while two events exhibited subhorizontal orientations. Considering the challenges in determining the rupture plane associated with the subducting slab, the densely deployed national seismic networks in Java are expected to provide valuable insights into the dynamics of the subduction zone. By elucidating the source characteristics and rupture behavior of these intermediate-depth events, our study offers valuable insights for future seismic hazard assessments, particularly for densely populated regions of Java, Indonesia.

1. Introduction

The Java subduction zone is recognized as one of the most seismically active regions globally and has experienced numerous destructive earthquakes. A characteristic of this subduction zone is the absence of significant megathrust events with a moment magnitude (M_W) $\geq$ 8 (Newcomb and McCann, 1987; Okal, 2012). The convergence direction within the Java subduction zone is nearly perpendicular to the plate boundary. The southern region of Java, Indonesia (Fig. 1) is part of the Sunda Arc, where the Australian Plate converges with the Eurasian Plate at a convergence rate of ~68 mm/yr (Koulali et al., 2017; Simons et al., 2007; Tregoning et al., 1994). Notably, the southwestern part of Java undergoes a transition from oblique subduction along Sumatra to orthogonal convergence along Java. Fig. 1 shows the seismicity from 1998 to 2017 obtained from the International Seismological Centre Engdahl-van der Hilst-Buland (ISC-EHB) catalog with a depth resolution of approximately 5 km (Engdahl et al., 2020). This figure shows that the seismicity primarily occurs in the fore-arc region. Notably, earthquakes with magnitudes greater than 6 are primarily concentrated at an intermediate-depth on the subduction zone.

Some active faults and volcanoes have formed along Java Island due to subduction of the Australian Plate beneath the Eurasian Plate, which gives this region a complex tectonic structure. The geometry of the Wadati–Benioff zone shows that the north-dipping Java slab exhibits a ~40° dip extending to 300 km depth, an aseismic region between 300 km and 400 km, and a steep dip up to 600 km (Chen et al., 2004),

* Corresponding author at: Taiwan International Graduate Program (TIGP) Earth System Science, Academia Sinica and National Central University, Room 7008, RCEC Building, No. 128, Section 2, Yanjiuyuan Rd., Nangang, Taipei 115, Taiwan.
E-mail address: megawati@g.ncu.edu.tw (M. Megawati).

https://doi.org/10.1016/j.jseaes.2024.106040
Received 13 November 2023; Received in revised form 6 January 2024; Accepted 25 January 2024
Available online 1 February 2024

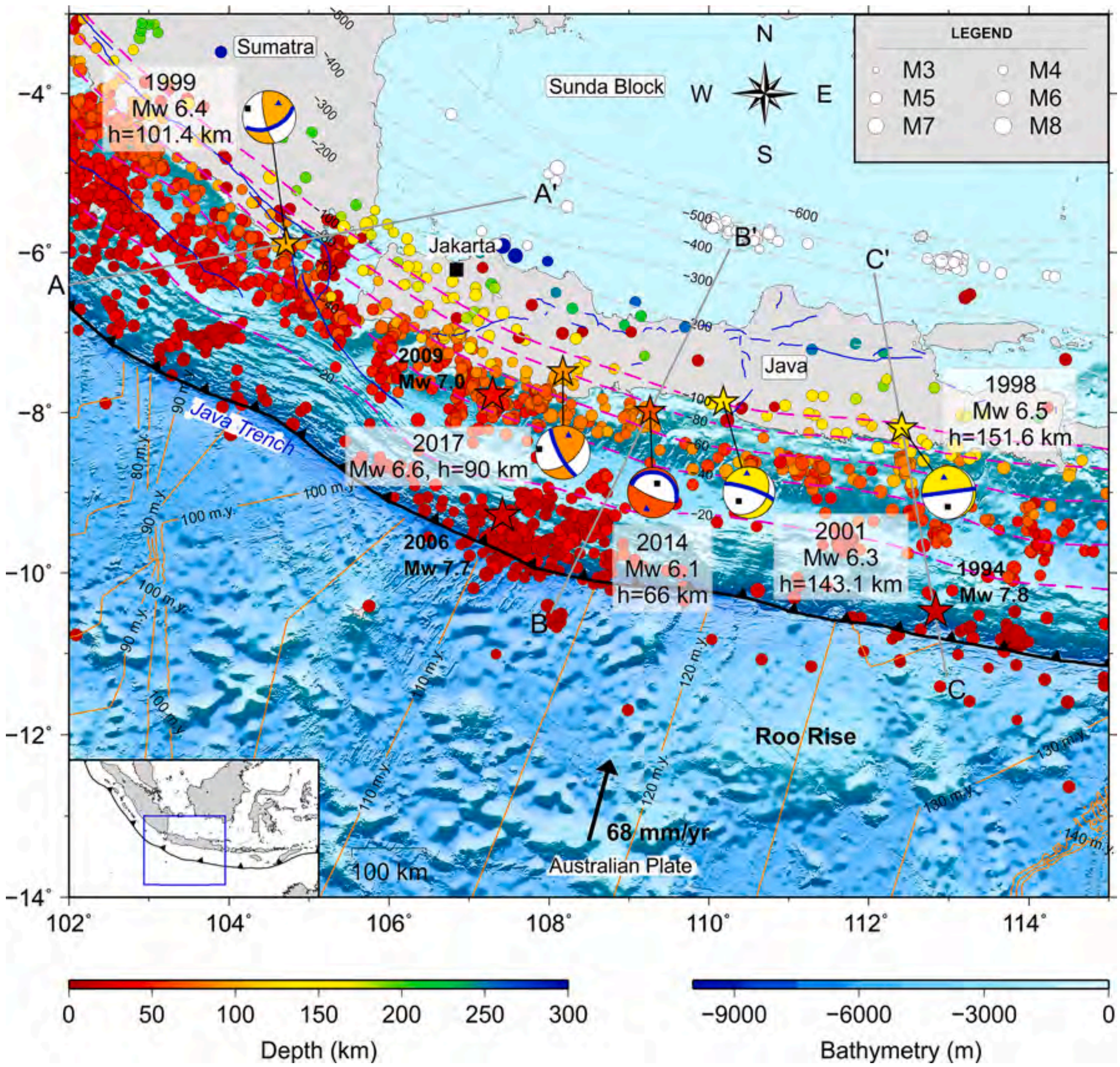

Fig. 1. Tectonic setting and background seismicity of the study area. The seismicity was retrieved from the ISC-EHB catalog (Engdahl et al., 2020) from 1998 to 2017. The colored stars with focal mechanisms show the epicenters of the five analyzed events, color-coded based on depth (bottom left scale). The focal mechanisms are the optimal solutions from our preliminary inversion tests which utilized the GCMT database (Ekström et al., 2012). The thick blue lines on each beachball indicate the preferred fault planes identified by directivity analysis, whereas black squares and blue triangles represent the orientation of the P- and T-axes, respectively. The solid blue lines represent the active faults from the 2017 Earthquake Source and Hazard Map of Indonesia (Irsyam et al., 2017). The cyan and gray contours denote the slab depths extracted from Slab2.0 (Hayes et al., 2018) with contour intervals of 20 km and 100 km, respectively. The brown lines indicate seafloor age contours (Seton et al., 2020). The black arrow denotes the Australian Plate motion relative to the Sunda Block. The blue rectangle in the inset map indicates the study area. Bathymetry data were retrieved from Global Multi-Resolution Topography (GMRT) (Ryan et al., 2009). Three profiles (AA', BB', and CC') are mostly perpendicular to the preferred fault planes from the epicenter. The 2001, 2014, and 2017 events were projected onto the BB' profile. (For interpretation of the references to color in this figure legend, the reader is referred to the web version of this article.)

aligning with previous tomography studies (Hall and Spakman, 2015; Widiyantoro et al., 2011). Hall and Spakman (2015) attributed the steep dip of this slab to the relatively old age of the subducted oceanic lithosphere (100–130 Ma; Seton et al., 2020) (Fig. 1). The Java subduction zone exhibits an along-strike variation of subducting age and seafloor topography, with an easterly increasing age of oceanic lithosphere and the presence of the Roo Rise to the east as it subducts beneath the forearc (Fig. 1; Kopp et al., 2006; Masson et al., 1990). Wang and Bilek (2014) suggested that, based on the rough seafloor and lack of significant earthquakes, creep is the primary mechanism operating in the Java subduction zone. Given the complex tectonic structure and high seismic activity, it is important to study the rupture processes and characteristics of intermediate-depth earthquakes in this subduction region.

Java Island is the most populous region in Indonesia with a population of ~153 million. In addition to the 2004 Sumatra-like megathrust earthquake, this region has experienced numerous historically significant and devastating tsunami earthquakes with magnitudes of approximately M7–M8 (Fig. 1, stars without associated focal mechanisms). For instance, the U.S. Geological Survey (USGS) reported that on 2 June 1994, an M_W 7.8 earthquake with a focal depth of 18.4 km occurred in the south of Java, resulting in a tsunami that claimed over 200 lives (Mori et al., 2007). Another powerful event took place on 17 July 2006, when an M_W 7.7 earthquake with a focal depth of 20.0 km (USGS) struck Pangandaran, south of Java, triggering a devastating tsunami that led to more than 600 fatalities and displaced over 75,000 individuals (Mori et al., 2007). On 2 September 2009, an M_W 7.0 intraslab earthquake with a focal depth of 46.0 km (USGS) occurred in Tasikmalaya, West Java. Although it did not generate a tsunami, it resulted in a coastal landslide (Sirait et al., 2020). This event caused over 80 deaths and led to 188,000 people being displaced (Gunawan et al., 2019).

Table 1
Source parameters of five intermediate-depth earthquakes (60–300 km depth) in southern Java, Indonesia, and its surrounding areas with moment magnitudes (M_W) ≥ 6.1 from 1998 to 2017.

Source parameter	1998 Java	1999 Southern Sumatra	2001 Java	2014 Java	2017 Java
Date (year-month-day) Origin time (UTC)	1998–09-28 13:34:30.5	1999–08-14 00:16:52.3	2001–05-25 05:06:10.7	2014–01-25 05:14:18.5	2017–12-15 16:47:58.2
Epicenter location from USGS	8.194°S; 112.413°E	5.885°S; 104.711°E	7.869°S; 110.179°E	7.986°S; 109.265°E	7.492°S; 108.174°E
Depth from USGS (km)	151.6	101.4	143.1	66	90
Seismic moment (Nm) from GCMT, (M_W)	7.65×10^{18}, (6.5)	5.13×10^{18}, (6.4)	3.17×10^{18}, (6.3)	2.10×10^{18}, (6.1)	8.45×10^{18}, (6.6)
Seismic moment (Nm) from this study, (M_W)	7.50×10^{18}, (6.5)	4.89×10^{18}, (6.4)	2.86×10^{18}, (6.2)	1.96×10^{18}, (6.1)	7.60×10^{18}, (6.5)
Focal mechanism strike/dip/rake from GCMT (°)	358/13/-176 263/89/-77	164/78/39 65/52/165	49/32/-158 300/79/-60	110/71/-88 282/19/-97	152/75/35 52/56/162
Focal mechanism strike/dip/rake from our preferred solution (°)*	1/13/-176 263/88/-77**	167/75/39 66/53/165**	37/32/-158 288/79/-60**	114/76/-88 284/14/-97**	152/77/35** 53/56/162
Rupture length L (km)	25	15	17.5	12	15
Rupture width W (km)	22.8	14.6	15.7	11.7	15.4
Peak slip (cm)	42.2	71.2	32.9	43.2	105.4
Average slip (cm)	17.3	29.6	14.1	18.6	42.5
Average rupture velocity (km/s)	2.6	2.8	2.7	2.9	2.7
Static stress drop (MPa)	0.8	2.1	0.9	1.7	3.0
Rupture length from directivity L_{dir}(km)	25	15	17.5	12	15
Rupture velocity from directivity v_{dir}(km/s)	4.0	2.5	3.25	2.25	4.0

* The rake angle was from the GCMT and was varied in the subfault in the finite-fault inversion.
** The preferred rupture plane obtained by directivity analysis.

While tsunamigenic earthquakes that occur on the subduction zones have attracted significant attention due to their destructive nature, it is important to recognize that intermediate-earthquakes (depth ~60–300 km) have also proven to be destructive for densely populated regions situated above subduction zones, including Java Island, Indonesia (Ye et al., 2014). Previous studies have investigated the source characteristics and rupture processes of intermediate-depth earthquakes in various regions worldwide, such as the Rat Islands, Alaska (Twardzik and Ji, 2015; Ye et al., 2014) and Peru (Liu and Yao, 2020; Ye et al., 2020). However, no studies have yet been conducted which focus on intermediate-depth earthquakes in Java. Therefore, it is crucial to address this research gap and study intermediate-depth earthquakes which occur in Java as they present unique challenges, because of their unclear faulting mechanisms, and have led to massive disasters.

Various models have been proposed to explain the physical mechanisms, including phase transitions (Liu and Zhang, 2015; Nakajima et al., 2013), dehydration embrittlement (Hacker et al., 2003; Jung et al., 2004; Okazaki and Hirth, 2016), transformational faulting (Ferrand et al., 2017; Kirby et al., 1996), and thermal shear instability (Kelemen and Hirth, 2007; Prieto et al., 2013). Kiser et al. (2011) suggested a dehydration embrittlement process associated with preferentially hydrated subhorizontal faults as a mechanism for intermediate-depth earthquakes. Previous studies have also investigated the mechanisms of intermediate-depth earthquakes related to stress release (Astiz et al., 1988; Fujita and Kanamori, 1981; Isacks and Molnar, 1971). According to Astiz et al. (1988), intermediate-depth earthquakes in Java occur in the uncoupled region due to the negative buoyancy of the subducted slab, with a relatively long and steeply dipping seismic zone.

In this study, we investigate the rupture processes of $M_W \geq 6.1$ intermediate-depth earthquakes in the southern region of Java and its surrounding areas (Fig. 1) from 1998 to 2017. Five earthquakes, which were well recorded by global seismic networks, were analyzed: the 28 September 1998 M_W 6.5 Java earthquake (USGS focal depth 151.6 km), the 14 August 1999 M_W 6.4 Southern Sumatra earthquake (USGS focal depth 101.4 km), the 25 May 2001 M_W 6.3 Java earthquake (USGS focal depth 143.1 km), the 25 January 2014 M_W 6.1 Java earthquake (USGS focal depth 66.0 km), and the 15 December 2017 M_W 6.6 Java earthquake (USGS focal depth 90.0 km (Table 1). To analyze these earthquakes, we employed a wavelet-based finite-fault inversion technique using teleseismic body waves and surface waves as described by Ji et al. (2002). We determined the ruptured fault planes based on waveform fits in the inversion and considered the effects of rupture directivity (Ji et al., 2002; Prieto, 2022; Prieto et al., 2009). By obtaining the finite-fault rupture models of earthquakes, we estimated source parameters such as rupture dimensions, rupture velocity, and stress drop. Additionally, we conducted directivity investigations to validate our results. The findings of this study contribute to our understanding of earthquake rupture behavior and its tectonic implications and provide valuable insights for seismic hazard assessments in Java Island, Indonesia.

2. The five Intermediate-Depth earthquakes and data

Fig. 1 shows the five selected intermediate-depth earthquakes that occurred in the southern region of Java and its surrounding areas from 1998 to 2017 with a magnitude (M_W) greater than 6.1. The hypocenter locations were obtained from the USGS database and the focal mechanisms from the Global Centroid Moment Tensor (GCMT) database (Ekström et al., 2012). According to the Agency for Meteorology, Climatology, and Geophysics of the Republic of Indonesia (BMKG) catalog for damaging earthquakes (2019), the earthquakes included in our study resulted in varying degree of damage and numbers of casualties. For instance, the earthquake which occurred on 15 December 2017 led to four fatalities, 11 serious injuries, 25 minor injuries, and damage to 2,935 houses and nearly one hundred buildings. The 28 September 1998 event caused one fatality, destroyed 38 houses, and damaged more than 62 houses and several buildings. The 25 January 2014 event resulted in damage to hundreds of houses. Despite the fact that these earthquakes occurred offshore, the occurrence of intermediate-depth M6+earthquakes highlights the need for further attention to seismic hazard assessment in Indonesia.

The seismicity data used in this study were retrieved from the ISC-EHB catalog (Engdahl et al., 2020) covering the period from 1998 to 2017 (Fig. 1). This catalog provides precise information on relocated events, along with their spatial resolution, from 1964 to 2019. Given that BMKG only had modern seismic networks after 2009, our study focused on teleseismic waveforms obtained from the Incorporated Research Institutions for Seismology Data Management Center (IRIS DMC) within an epicentral distance range of 30° to 90° to reduce the complexity of the Earth's structure for typical moderate-magnitude earthquakes (Hao et al., 2013; Twardzik and Ji, 2015).

3. Data processing and methods

Data preprocessing included removing instrument responses through a deconvolution process using Seismic Analysis Code (SAC) software (Goldstein and Snoke, 2005). Velocity seismograms were then integrated to obtain the displacement seismograms, and a coordinate rotation was applied to obtain the horizontal component of the shear waves (SH). It is worth noting that SH-waves exhibit lower signal-to-noise ratios and higher arrival-time uncertainty. To address this issue, weighting was applied during the inversion, giving SH-waves half the weight of P-waves. Long-period surface waves were assigned double the weight of P-waves since Green's functions are more suitable for long-period surface waves than for body waves (Shao et al., 2011).

The displacement body waves were band-pass filtered between 0.005 Hz and 1 Hz, while long-period surface waves were filtered between 0.004 Hz and 0.006 Hz (Hao et al., 2013). The waveform length varied according to the magnitude of each earthquake. The sampling intervals for displacement seismograms were 0.2 s and 4 s for body waves and surface waves, respectively. The arrival times of P- and SH-waves were estimated using the IASP91 travel-time table (Kennett and Engdahl, 1991) and manually adjusted for the inversion process. As an example, Fig. 2 shows the distribution of the teleseismic broadband stations used in this study for body waves (P and SH) and surface waves (Rayleigh and Love) for the 15 December 2017 Java earthquake. The same stations were considered for all five earthquakes analyzed in this study. The stations generally provided good azimuthal coverage of the earthquakes and offered satisfactory signal-to-noise ratios of waveforms for the analysis.

In this study, we employed a kinematic finite-fault inversion method that utilized teleseismic body waves and surface waves as described by Ji et al. (2002). This method relies on assumed fault geometry and has been widely employed in previous studies (Hao et al., 2013; Hsieh et al., 2016; Ji et al., 2003; Lin et al., 2019; Shao et al., 2011). The inversion procedure involved a nonlinear waveform inversion using a wavelet transform and a simulated annealing method. The wavelet transform played a crucial role in converting observed and synthetic waveforms into a combined representation of the time and frequency domain. This transformation facilitated comparison and analysis of wavelet coefficients between observed and synthetic waveforms. A simulated annealing method, known as the heat-bath algorithm, was used to search for the optimal finite-fault model. This algorithm enabled an efficient search for the best-fit finite-fault model by minimizing the misfit of wavelet coefficients. From this inversion, we simultaneously determined the slip amplitude, slip direction (rake angle), rupture initiation time, and the asymmetric slip rate function (rise time) of each subfault.

3.1. Fault Geometry, source time Function, and velocity structure

Firstly, we conducted a series of preliminary inversion tests to determine the strike and dip of the earthquakes, with variation within $\pm 20^\circ$, using the GCMT solution. The fault geometry was justified based on the minimum misfit between the synthetic and observed waveforms. For each earthquake, a single rectangular fault plane was considered, with the strike and dip values derived from the minimum misfit while the rake angle was taken directly from the GCMT solution. Initially, the rupture dimension was estimated using the scaling relation of Strasser et al. (2010) and then adjusted visually to ensure a well-resolved slip distribution on the fault plane. In our preliminary finite-fault inversions, high slips around the fault plane edges were identified, and we expanded the fault plane if the slip values around the fault plane edges were significant (Zheng et al., 2020). All slip areas should be completely distributed on the fault plane. In addition, fault plane sizes were reconsidered to ensure minimum smearing effects on the resolved slip models (Hsieh et al., 2016).

In this inversion approach, the asymmetric cosine function was used to estimate the derivative of the source time functions (Ji et al., 2003). The slip rate in each subfault was assigned using the value of the starting time (t_s) and ending time (t_e) of this asymmetric cosine function (Ji et al., 2003). The inverted rise time for each subfault was computed by summing these times ($t_s + t_e$). The rise time value was constrained within the range of 0.5 to 5 s. Variation within a certain range was allowed for the rupture velocity, which refers to the temporal constraint (Shao et al., 2011). In this study, the reference rupture velocity was set at 2.5 km/s, with a range of 1.25 km/s to 3.75 km/s. The specific rupture velocity of each event was further determined in the directivity analysis. The rake angle (slip vector) for each subfault was searched within ±30° of the GCMT rake as a reference value.

The velocity model used in the inversion was extracted from the Crust2.0 global 1D velocity model (Bassin et al., 2000) and the Preliminary Reference Earth Model (PREM; Dziewonski and Anderson, 1981). This velocity model provides information about the Earth's structure in the source region. Attenuation effects on the seismic waveform at teleseismic distances were accounted for using attenuation constants for P- and SH-waves ($t_\alpha^* = 1.0\,\mathrm{s}$ and $t_\beta^* = 4.0\,\mathrm{s}$, respectively), where t^* is the time-constant of the body wave attenuation operator (Futterman, 1962). Synthetic waveforms for teleseismic body waves were calculated using first motion approximation using the generalized ray theory method (Langston and Helmberger, 1975; Helmberger, 1983), while the synthetic waveforms for long-period surface waves were computed using the normal mode superposition algorithm (Gilbert et al., 1975; Shao et al., 2011).

The objective function defined via wavelet decomposition for the inversion included the L1 + L2 norm for low-frequency and cross-correlation for high-frequency signals, providing a multi-scale solution of slip distribution and ensuring more reliable results (Ji et al., 2002). This function, denoted as $E(m)$, was defined as a cumulative misfit between the observed and synthetic waveforms, incorporating additional terms for seismic moment, slip smoothness, and rupture front regularity as:

$$E(m) = E_{wf} + \lambda_1 E_{moment} + \lambda_2 E_{smooth} + \lambda_3 E_{time} \quad (1)$$

where $E_{wf}(m)$ indicates the cumulative misfit between the observed and synthetic waveforms. To stabilize the inversion process, three types of regularization were employed: E_{moment}, which minimizes the discrepancy between the inverted seismic moment and the value from long-period seismic data, such as the GCMT solution (Ji et al., 2002); E_{smooth}, which minimizes the discrepancy between the slip values on neighboring subfaults using a Laplacian operator (Ji et al., 2002); E_{time}, which suppresses the irregularity in the rupture front (Shao et al., 2011). The regularization terms were weighted using λ_1, λ_2, and λ_3, which were all set to 0.1 in our study.

The optimum slip model for each earthquake was obtained through a rigorous process involving initial finite-fault inversions and meticulous reviews to address uncertainties in our analysis. These reviews included the removal of poor-quality stations, manual adjustment of waveform picking in time, and visual refinement of the fault plane size. We show these reviews using an example of the most significant magnitude of our analyzed events, namely the 15 December 2017 M_W 6.6 Java earthquake in supplementary Figs. S21-S25. Additionally, comprehensive preliminary inversion tests were conducted to validate the fault geometry based on the minimum misfit, utilizing the available data (see supplementary information for Figs. S1, S5, S9, S13, and S17).

3.2. Directivity analysis and stress drop

To enhance justification of the ruptured fault plane, we employed directivity analysis in addition to general waveform fitting of two fault planes. The directivity analysis involved calculating the apparent source time functions (ASTFs) with varying rupture velocities to determine the likely fault plane of the target earthquakes. The ASTFs were calculated using the following equation (Ben-Menahem and Singh, 1981; Cesca et al., 2011):

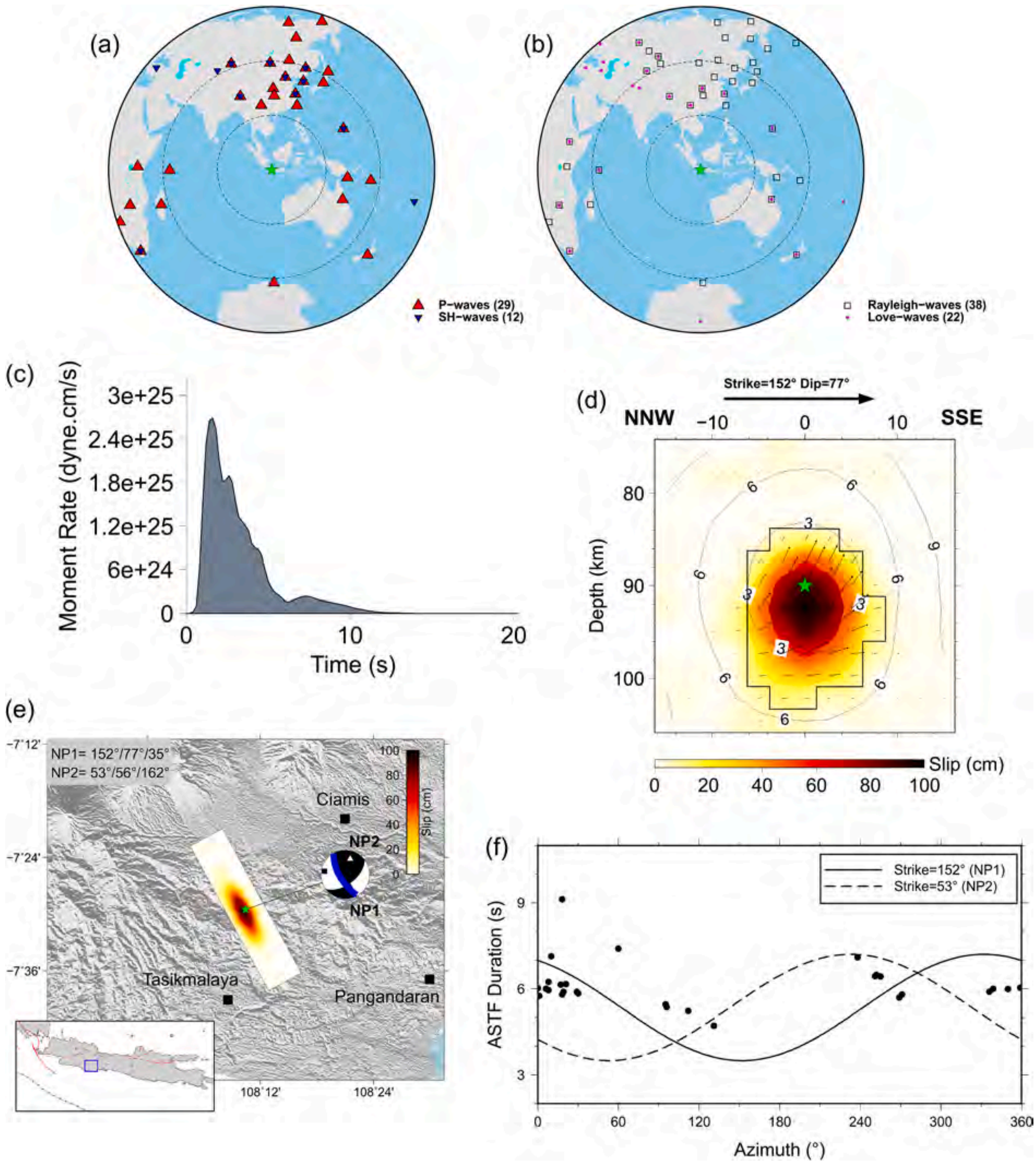

Fig. 2. The finite-fault rupture model for NP1 and the directivity analysis of the 15 December 2017 Java earthquake (M_W 6.6). (a, b) Distribution of the teleseismic stations used for the finite-fault inversion for body waves and surface waves, respectively; red and blue reverse triangles represent the stations that recorded P-waves and SH-waves, respectively; black squares and magenta circles represent Rayleigh-wave and Love-wave stations, respectively; the green star indicates the epicenter of the earthquake; dashed circles indicate the epicenter distance at 30° intervals. (c) Source time function (STF) describing moment rate evolution with time after the earthquake origin. (d) Slip distribution on the fault plane; the green star indicates the hypocenter; contours show the rupture propagation time at 3 s intervals; black arrows indicate the slip size and slip (rake) direction of each subfault; the thick black line indicates the rupture area (A) of subfaults with slip larger than 10 % of the maximum slip (Hao et al., 2017); the large black arrow denotes the strike direction. (e) Surface projection of slip distribution in (d) superimposed on topography; the green star represents the epicenter of the earthquake; the beachball indicates the optimal focal mechanism solution from our preliminary inversion tests; the thick blue line on the beachball denotes the preferred fault plane from directivity analysis, whereas the black square and white triangle represent the orientation of the P-axis and T-axis, respectively; the black squares show the damage caused by this earthquake to the cities of Tasikmalaya, Ciamis, and Pangandaran in West Java; the inset map indicates the location of the enlarged figure (blue square) and active faults (red lines) obtained from the 2017 Earthquake Source and Hazard Map of Indonesia (Irsyam et al., 2017). (f) The fitting curves between the observed ASTFs (solid circles) and the calculated Δt for two nodal planes, NP1 and NP2, respectively, obtained from directivity analysis; the solid and dashed black lines show the calculated Δt for NP1 and NP2, respectively. (For interpretation of the references to color in this figure legend, the reader is referred to the web version of this article.)

$$\Delta t = t_r + \frac{L}{v_R} - \frac{L\cos(\varphi - \theta)}{v_P} \tag{2}$$

where t_r is the rise time, L is the rupture length, v_R is the rupture velocity, v_P is the P-wave velocity of the region, φ is the unilateral rupture propagation direction, and θ is the station's azimuth. The azimuth-dependent source duration can be used to determine earthquake directivity.

The ASTFs were computed using the vertical component of teleseismic waveforms. The synthetic seismograms, which were generated based on the optimal solution of the preliminary inversion result and the IASP91 velocity model (Kennett and Engdahl, 1991), were retrieved from the IRIS Synthetics Engine (Syngine) (https://ds.iris.edu/ds/products/syngine/). The multitaper method (Prieto, 2022; Prieto et al., 2009) was utilized for frequency domain deconvolution to obtain the ASTFs. This method computes multitapered Fourier spectra of observed and synthetic data in the frequency domain, implements the spectral division, and then converts the spectral ratio back to the time domain by performing an inverse Fourier transform thereby yielding the source time function (STF). This method has been utilized in previous studies (Semmane et al., 2017; Viegas, 2012) for ruptured fault plane determination.

We used a time window of 40 s (5 s before to 35 s after the P-wave arrival); however, for the 15 December 2017 event, we instead used a time window of 35 s (5 s before to 30 s after the P-wave arrival) to avoid negative values of the ASTF, which can lead to non-physical solutions (Dębski, 2008). We utilized the same vertical component of teleseismic waveforms as those used in the finite-fault inversion. By manually picking the start and end times of the ASTFs, we measured the apparent source duration and compared it with the calculated Δt. The fitting between the observed ASTFs and the calculated Δt was evaluated using the L1-norm misfit (López-Comino et al., 2015) as the objective function:

$$L_1 = \sum_{O_i=1}^{O_i=N} \frac{|obs_i - calc_i|}{N} \tag{3}$$

where *obs* represents the observed data, *calc* is the calculated Δt, and N is the number of data points. The rupture length and rise time were fixed based on finite-fault results, and P-wave velocity was set at 8.1 km/s as the average velocity for events at these depths. Considering the average rupture velocity obtained from finite-fault inversion in our study, we tested various rupture velocities between 2 km/s and 4 km/s at intervals of 0.25 km/s, fitting the strikes of both nodal planes (NP1 and NP2) with the observed ASTFs, as shown in supplementary Figs. S4a, S8a, S12, S16, and S20.

Estimation of static stress drop is known to be challenging and subject to significant uncertainty (Ye et al., 2016). However, for intermediate-depth earthquakes, a relatively high static stress drop is typically observed (Ye et al., 2020). We followed the approach used in previous studies to obtain the effective rupture size from finite-fault models by removing subfaults with poorly resolved models. Specifically, we considered subfaults with inverted slip values larger than 10% of the maximum slip (Hao et al., 2013, 2017; Somerville et al., 1999; Ye et al., 2016) as significant slip subfaults (Hao et al., 2017; Yen and Ma, 2011). The stress drop was calculated for each event using the equation $\Delta\sigma_s = C\frac{M_0}{AL}$ (Kanamori and Anderson, 1975), where C is a nondimensional constant, M_0 is the seismic moment, A is the fault area, and L is the smaller characteristic length of the fault (either fault length or width). We used $C = \frac{7\pi}{16}$ for a circular-shaped rupture. The fault area (A) was determined based on the total dimension of subfaults with slip larger than 10% of the maximum slip.

4. Results

4.1. The 15 December 2017 M_W 6.6 Java earthquake

The M_W 6.6 earthquake occurred in Tasikmalaya, West Java, at 16:47:58 UTC on 15 December 2017. The USGS reported the epicenter location as 7.492°S and 108.174°E, with a focal depth of 90 km. We conducted preliminary tests of the focal mechanism (strike ϕ and dip δ), defining two nodal planes, which had the same dimensions (32.5 km along strike and 32.5 km down-dip) as a rectangular fault plane. The fault plane was divided into 169 subfaults, each with a grid size of 2.5 km × 2.5 km. In this study, the grid sizes were considered in relation to the rise time (local slip duration) and expected rupture velocity. In addition, the grid sizes were related to the number of unknown parameters that influence the quality of the inversion results. We utilized seismograms from 46 teleseismic stations, including 29 P-wave, 12 SH-wave, 38 Rayleigh-wave, and 22 Love-wave recordings (Fig. 2a and 2b), to invert the finite-fault slip model of this event. The length of displacement waveforms for each body wave was 20 s from the P-wave first arrival and 3600 s for the long-period surface waves from the origin time. We performed finite-fault inversions, varying the strike and dip by $\pm 20^\circ$ of the GCMT solution, to find the best fit (Fig. S1). The final optimal solution for strike, dip, and rake obtained was NP1 ($\phi = 152^o$, $\delta = 77^o, \lambda = 35^o$) and NP2 ($\phi = 53^o, \delta = 56^o, \lambda = 162^o$), which is in good agreement with the GCMT solution (Table 1).

The synthetic waveforms (Figs. S2 and S3) demonstrate good agreement with the observed waveforms, with a minimum cumulative misfit of 0.198 for NP1 and 0.202 for NP2. Although the difference in misfit values between these two fault planes is small, this suggests that NP1 might be a preferred rupture plane. Fig. 2c and 2d show the STF and slip distribution of NP1, respectively. The rupture displayed a simple triangular shape with a total rupture duration of approximately 11 s, with the primary moment release occurring within the first 6 s. The rupture was initiated from a depth of 90 km, with a maximum slip of 105.4 cm in the down-dip direction. Considering the region with slip larger than 10% of the maximum slip, the average slip of this event was approximately 42.5 cm. The corresponding rupture length from the finite-fault result was $L = 15$ km. The slip vectors revealed an oblique mechanism, dominated by unilateral down-dip rupture propagation with an average rupture velocity of approximately 2.7 km/s. The total seismic moment for NP1 was 7.60×10^{18} Nm, equivalent to an M_W 6.5 according to Hanks and Kanamori (1979), slightly lower than the M_W of 6.6 obtained from the GCMT solution. By considering the fault area (A) encompassing subfaults with slip larger than 10% of the maximum slip (Fig. 2d), the static stress drop ($\Delta\sigma_s$) was determined to be approximately 3.0 MPa. Additionally, Fig. 2e shows the map view of this slip distribution where the preferred rupture plane is near-vertical, which resulted in damage to the cities of Tasikmalaya, Ciamis, and Pangandaran in West Java.

Fig. 2f shows the fitting curves between the observed ASTFs and the calculated Δt for two nodal planes, NP1 and NP2, respectively, obtained from directivity analysis. These curves represent the results obtained after testing various rupture velocities (as shown in Fig. S4a) and selecting the minimum fit. The analysis reveals that the near-vertical fault plane (NP1) exhibits a lower L1-misfit of 0.96 compared with the subhorizontal fault plane (NP2), confirming the preferred fault plane identified through finite-fault inversion. However, it is important to note that the misfit curve for determining the rupture velocity of NP1 (as shown in Fig. S4a) does not exhibit a stable minimum. This highlights the difficulty in definitively determining the rupture velocity for this steep-angle fault plane, despite the misfit curve suggesting a relatively fast rupture velocity of up to 4 km/s, which is nearly equivalent to 90% of the shear wave velocity (~4.5 km/s) at the corresponding depth. In comparison, Fig. S4b shows the fitting curves of the directivity analysis for the rupture velocity determined from the finite-fault inversion,

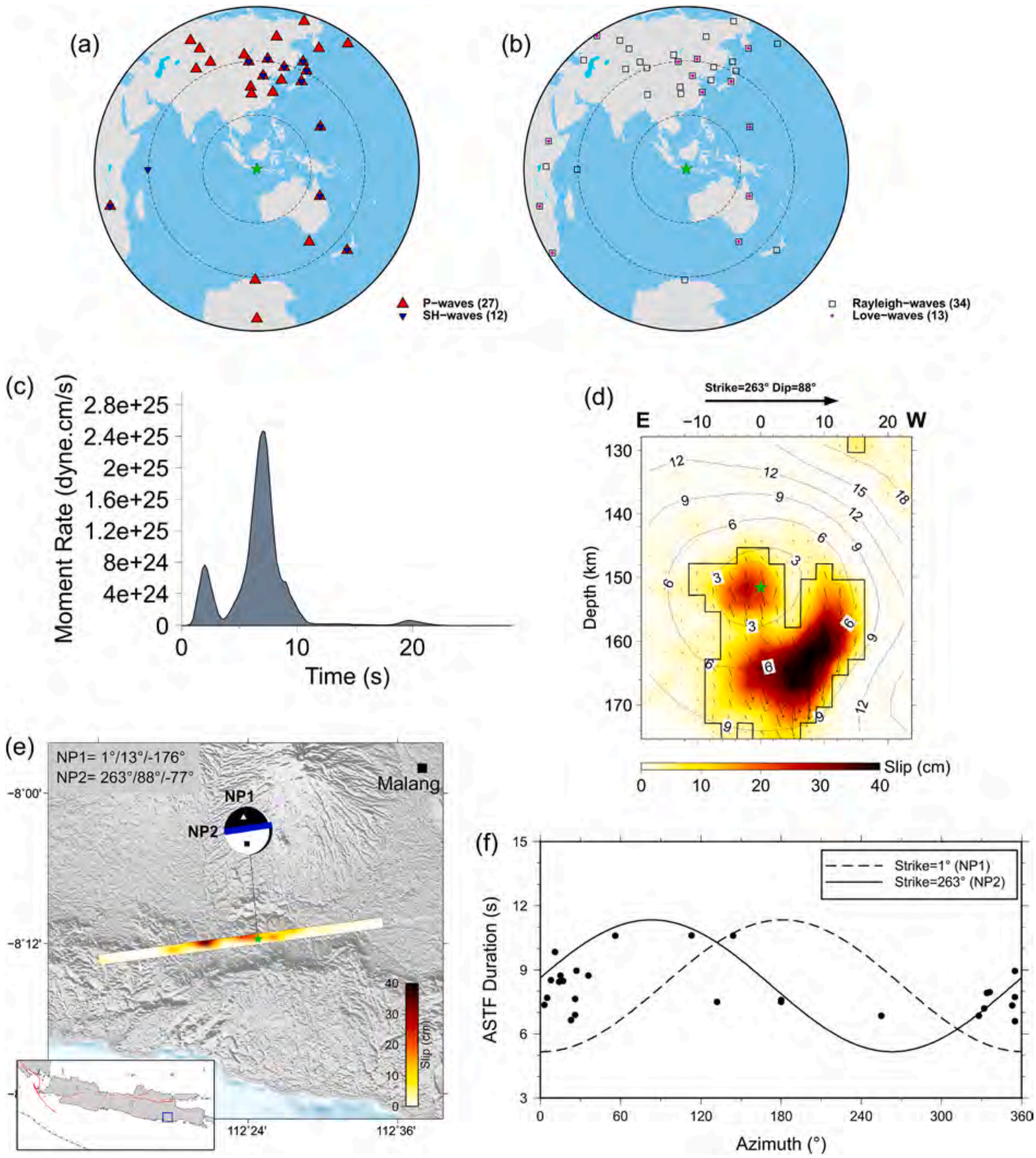

Fig. 3. The finite-fault rupture model for NP2 and the directivity analysis of the 28 September 1998 Java earthquake (M_W 6.5). The black square in (e) shows the damage to the city of Malang in East Java caused by this earthquake. The dashed and solid black lines in (f) show the calculated Δt for NP1 and NP2, respectively. Other captions and symbols are as per Fig. 2.

which is 2.7 km/s. Although the difference in misfit values between these two preferred models (rupture velocity of 2.7 km/s for NP2 and 4.0 km/s for NP1) is small, visual examination (Fig. 2f and Fig. S4b) suggests that the fitting curve for NP1 with a rupture velocity of 4.0 km/s provides a better fit. This is supported by its smaller misfit value (Fig. S4a). However, it is important to acknowledge the difficulty in definitively determining the rupture velocity.

4.2. The 28 September 1998 M_W 6.5 Java earthquake

The M_W 6.5 earthquake occurred in the southern part of East Java at 13:34:30 UTC on 28 September 1998. According to the USGS, the epicenter location is 8.194°S and 112.413°E, with a focal depth of 151.6 km. Preliminary tests of the focal mechanism (strike ϕ and dip δ) (Fig. S5) were conducted to identify two nodal planes represented by rectangular fault planes with the same dimensions of 42.5 km along strike and 47.5 km down-dip. The fault plane was divided into 323 square subfaults with a grid size of 2.5 km × 2.5 km. We used 35 teleseismic stations, including 27 P-wave, 12 SH-wave, 34 Rayleigh-wave, and 13 Love-wave seismograms (Fig. 3a and 3b). The displacement waveforms for each body wave had a length of 25.6 s from the P-wave first arrival, while the long-period surface waves were analyzed up to 3600 s from the origin time. For the 1998 event, the optimal solution for strike, dip, and rake of the two nodal planes was NP1 ($\phi = 1^o, \delta = 13^o$,

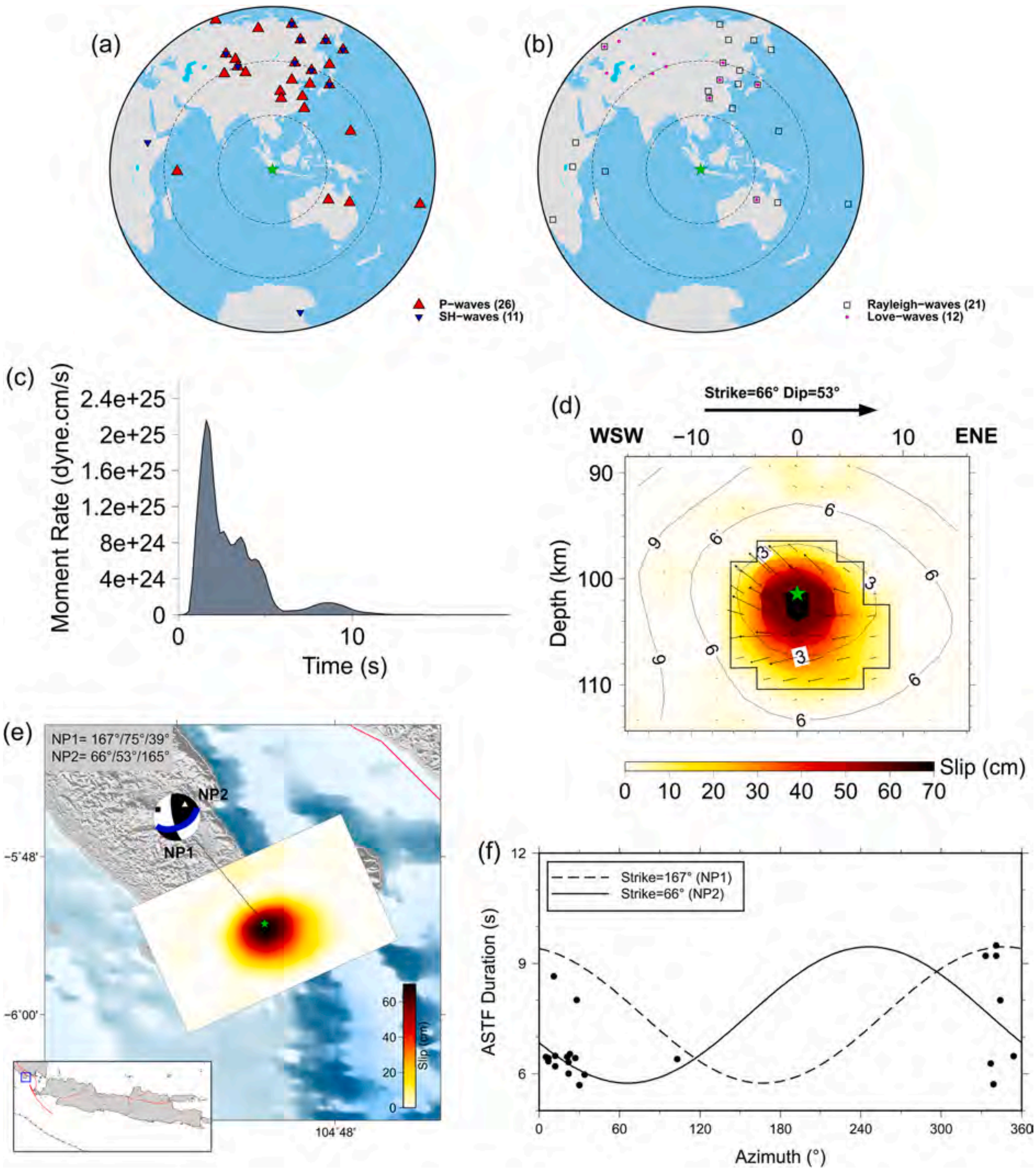

Fig. 4. The finite-fault rupture model for NP2 and the directivity analysis of the 14 August 1999 Southern Sumatra earthquake (M_W 6.4). The dashed and solid black lines in (f) show the calculated Δt for NP1 and NP2, respectively. Other captions and symbols are as per Fig. 2.

$\lambda = -176^o$) and NP2 ($\phi = 263^o, \delta = 88^o, \lambda = -77^o$), as listed in Table 1.

The synthetic waveforms (Figs. S6 and S7) demonstrate good agreement with the observed waveforms, with a minimum cumulative misfit of 0.242 for NP2. Fig. 3c and 3d show the STF and slip distribution for NP2, respectively. The STF exhibits a double-peak, indicating that the rupture commenced with a small initiation and then propagated with larger slip over a total duration of approximately 11 s. The rupture was initiated from a depth of approximately 151.6 km with a maximum slip of 42.2 cm in the down-dip direction. The average slip of this event was approximately 17.3 cm. The slip vectors depicted an oblique mechanism, characterized by a predominately unilateral down-dip rupture propagation at an average rupture velocity of approximately 2.6 km/s. The corresponding rupture length from the finite-fault slip model of this event was $L = 25$ km. The total seismic moment for NP2 was estimated to be 7.50×10^{18} Nm, equivalent to an M_W 6.5 earthquake based on Hanks and Kanamori (1979). The moment magnitude calculated using the seismic moment of the earthquake was similar to the moment magnitude reported in the GCMT solution. By considering the fault area (A) based on the subfaults with slip larger than 10% of the maximum slip (Fig. 3d), the static stress drop ($\Delta\sigma_s$) was estimated to be approximately 0.8 MPa. The slip distribution is shown in map view in Fig. 3e, illustrating the narrow nature of the slip pattern due to the near-vertical rupture plane. Despite the narrow slip pattern, this event still resulted in damage to the city of Malang in East Java.

Fig. 3f shows the fitting curves between the observed ASTFs and the calculated Δt for two nodal planes, NP1 and NP2, respectively, obtained

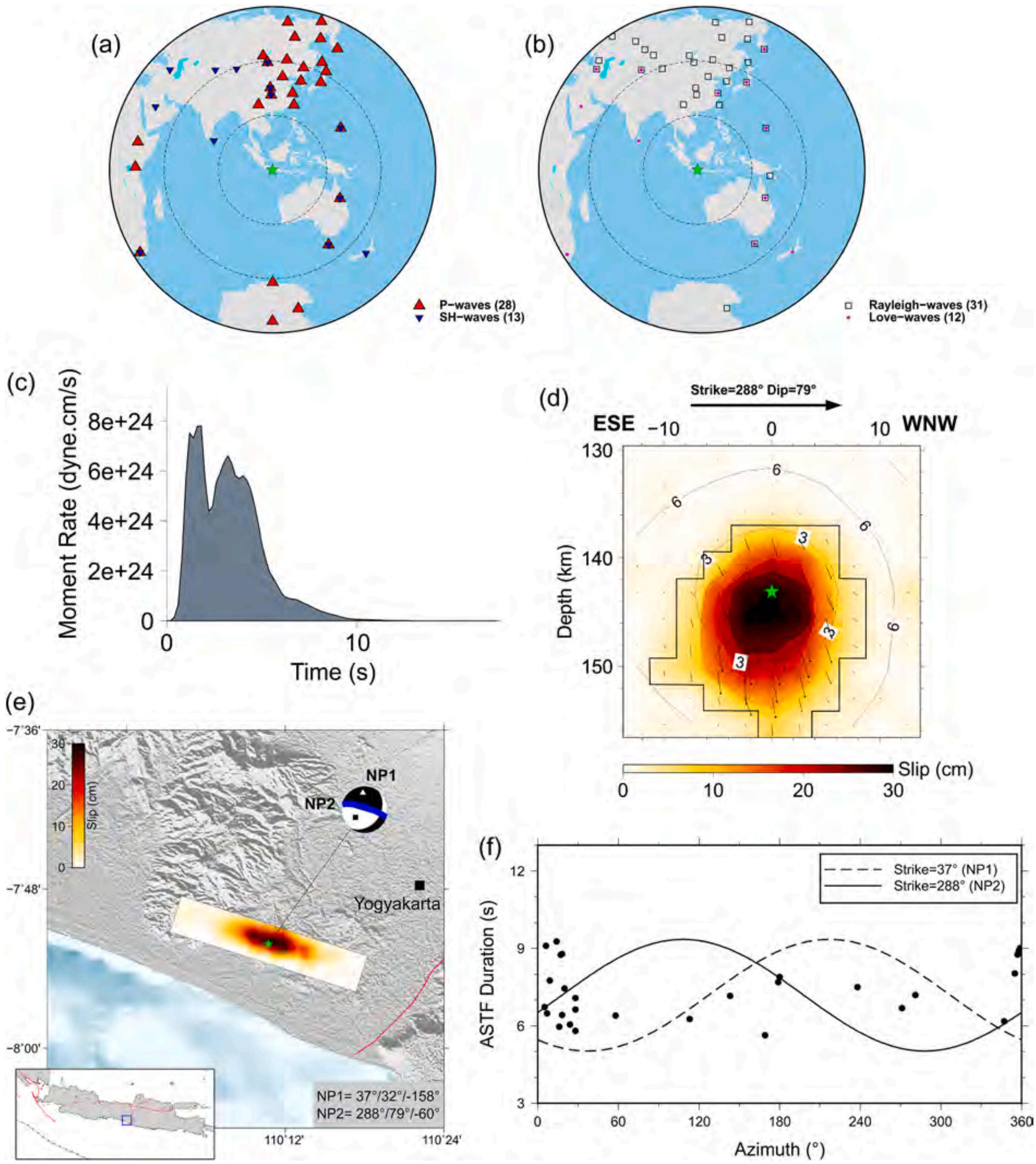

Fig. 5. The finite-fault rupture model for NP2 and the directivity analysis of the 25 May 2001 Java earthquake (M_W 6.3). The black square in (e) shows the damage to the city of Yogyakarta caused by this earthquake. The dashed and solid black lines in (f) show the calculated Δt for NP1 and NP2, respectively. Other captions and symbols are as per Fig. 2.

by directivity analysis. These curves represent the results obtained after testing various rupture velocities (as shown in Fig. S8a) and selecting the minimum fit. The analysis revealed that the near-vertical fault plane (NP2) exhibited a lower L1-misfit of 1.09 compared with the sub-horizontal fault plane (NP1), confirming the results from finite-fault inversion. However, similar to the 15 December 2017 earthquake, the misfit curve for determining the rupture velocity of NP2 (as shown in Fig. S8a) does not exhibit a stable minimum. This again highlights the difficulty in definitively determining the rupture velocity for this steep-angle fault plane, despite the misfit curve also suggesting a relatively fast rupture velocity of up to 4 km/s. In comparison, Fig. S8b also shows the fitting curves of the directivity analysis for the rupture velocity determined from the finite-fault inversion, which is 2.6 km/s. Visual examination of Fig. 3f and Fig. S8b suggests that the fitting curve for NP2 with a rupture velocity of 4.0 km/s provides a better fit, which is supported by its smaller misfit value (Fig. S8a). However, as with the 15 December 2017 earthquake, it is important to acknowledge the difficulty in definitively determining the rupture velocity for near-vertical fault planes.

4.3. The 14 August 1999 M_W 6.4 southern Sumatra earthquake

The M_W 6.4 earthquake occurred in the southwest of Bandar Lampung, the southern part of Sumatra, at 00:16:52 UTC on 14 August 1999.

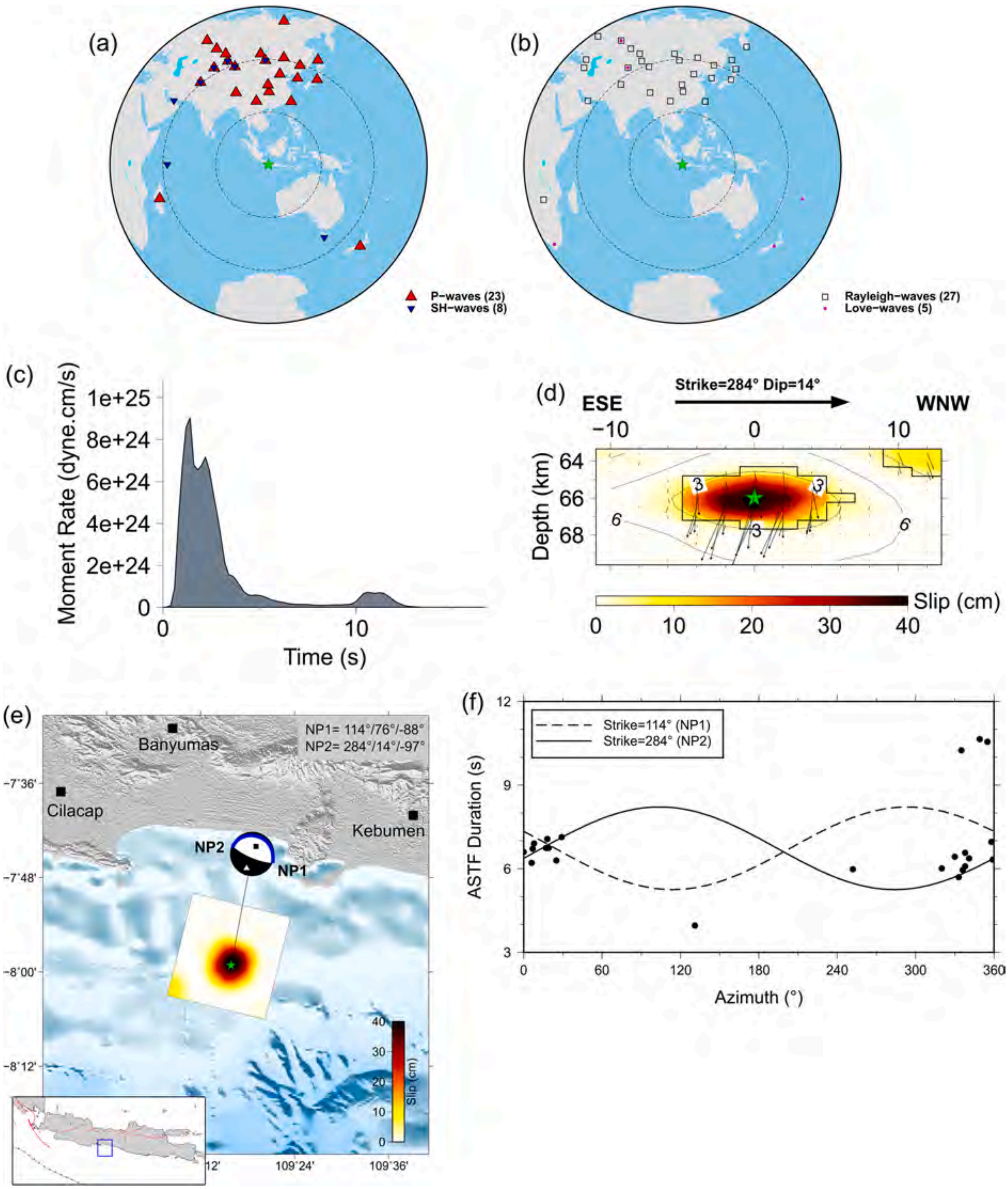

Fig. 6. The finite-fault rupture model for NP2 and the directivity analysis of the 25 January 2014 Java earthquake (M_W 6.1). The black squares in (e) show the damage to the cities of Kebumen, Banyumas, and Cilacap in Central Java caused by this earthquake. The dashed and solid black lines in (f) show the calculated Δt for NP1 and NP2, respectively. Other captions and symbols are as per Fig. 2.

According to the USGS, the epicenter location was 5.885°S and 104.711°E, with a focal depth of 101.4 km. Preliminary tests of the focal mechanism (strike ϕ and dip δ) were conducted (Fig. S9) and defined the two nodal planes of the rectangular fault plane with the same dimensions of 32.5 km along strike and 32.5 km down-dip. The fault plane was divided into 169 subfaults with a grid size of 2.5 km × 2.5 km. We used 33 teleseismic stations, including 26 P-wave, 11 SH-wave, 21 Rayleigh-wave, and 12 Love-wave seismograms (Fig. 4a and 4b). The displacement waveforms for each body wave had a length of 20 s from the P-wave first arrival, while the long-period surface waves were analyzed up to 3600 s from the origin time. For the 1999 event, the optimal solution for strike, dip, and rake of the two nodal planes was NP1 ($\phi = 167^o, \delta = 75^o, \lambda = 39^o$) and NP2 ($\phi = 66^o, \delta = 53^o, \lambda = 165^o$) (Table 1).

The synthetic waveforms (Figs. S10 and S11) demonstrate good agreement with the observed waveforms with a minimum cumulative misfit of 0.207 for NP2, suggesting a preferred subhorizontal fault plane. Fig. 4c and 4d show the STF and slip distribution for NP2, respectively. The STF exhibits a simple rupture process with a total duration of approximately 11 s, with the primary moment release occurring in the first ~6 s. The rupture initiated from a depth of approximately 101.4 km, with a maximum slip of 71.2 cm in the down-dip direction. The average slip of this event was approximately 29.6 cm. The slip vectors depicted an oblique mechanism, characterized by a predominantly unilateral down-dip rupture propagation at an average rupture velocity of approximately 2.8 km/s. The rupture length was $L = 15$ km. The total seismic moment for NP2 was estimated to be 4.89×10^{18} Nm, equivalent to an M_W 6.4 earthquake based on Hanks and Kanamori (1979). The moment magnitude calculated using the seismic moment of the earthquake is similar to the moment magnitude reported in the GCMT solution. By considering the fault area (A) based on the subfaults with slip larger than 10% of the maximum slip (Fig. 4d), the static stress drop ($\Delta\sigma_s$) was estimated to be around 2.1 MPa. Fig. 4e shows the map view of this slip distribution of the subhorizontal fault plane (NP2).

Fig. 4f shows the fitting curves between the observed ASTFs and the calculated Δt for NP1 and NP2 after testing various rupture velocities in the directivity analysis. The results indicate that the subhorizontal fault plane (NP2) is a preferred fault plane, with an L1-misfit of 0.75, compared with that of the near-vertical fault plane (NP1) of 1.02 (Fig. S12), confirming the results from finite-fault inversion. Based on this analysis, we estimated a rupture velocity of 2.5 km/s as the best fit, which is comparable with that obtained from the finite-fault analysis of 2.8 km/s.

4.4. The 25 May 2001 M_W 6.3 Java earthquake

The M_W 6.3 earthquake occurred in the southern part of Java at 05:06:10 UTC on 25 May 2001. The epicenter location from the USGS was 7.869°S and 110.179°E, with a focal depth of 143.1 km. Preliminary tests of the focal mechanism (strike ϕ and dip δ) were conducted (Fig. S13) and defined the two nodal planes with a rectangular fault plane of 27.5 km along strike and 27.5 km down-dip. The fault plane was divided into 121 subfaults with a grid size of 2.5 km × 2.5 km. We used 40 teleseismic stations, including 28 P-wave, 13 SH-wave, 31 Rayleigh-wave, and 12 Love-wave seismograms (Fig. 5a and 5b). The displacement waveforms for each body wave had a length of 20 s from the P-wave first arrival, while the long-period surface waves were analyzed up to 3600 s from the origin time. For the 2001 event, the optimal solution for strike, dip, and rake for these two nodal planes was NP1 ($\phi = 37^o$, $\delta = 32^o, \lambda = -158^o$) and NP2 ($\phi = 288^o, \delta = 79^o, \lambda = -60^o$) (Table 1).

The synthetic waveforms (Figs. S14 and S15) demonstrate good agreement with the observed waveforms with a minimum cumulative misfit of 0.291 for NP2. Fig. 5c and 5d show the STF and slip distribution for NP2, respectively. The STF exhibits a simple rupture process with a total duration of about 10 s, with primary moment release occurring within the first ~6 s. The corresponding rupture length from the finite-fault result was $L = 17.5$ km. The rupture was initiated from a depth of approximately 143.1 km, with a maximum slip of 32.9 cm in the down-dip direction. The average slip of this event was approximately 14.1 cm. The slip vectors indicate an oblique mechanism, predominately characterized by unilateral down-dip rupture propagation with an average rupture velocity of approximately 2.7 km/s. The total seismic moment for NP2 was estimated to be 2.86×10^{18} Nm, which is equivalent to an M_W 6.2 earthquake based on Hanks and Kanamori (1979). The moment magnitude calculated using the seismic moment of the earthquake was slightly lower than the moment magnitude reported by the GCMT solution ($M_W = 6.3$). Using the fault area (A) with the total dimensions from the subfaults with slip larger than 10% of the maximum slip (Fig. 5d), the static stress drop ($\Delta\sigma_s$) was estimated to be approximately 0.9 MPa. Fig. 5e shows the map view of this slip distribution of the near-vertical fault plane, which resulted in damage to the city of Yogyakarta.

Fig. 5f shows the fitting curves between the observed ASTFs and the calculated Δt for NP1 and NP2 after testing various rupture velocities in the directivity analysis. This shows that the near-vertical fault plane (NP2) is a preferred fault plane as it displays an L1-misfit of 1.43 compared with that of the subhorizontal fault plane (NP1) of 1.61 (Fig. S16), confirming the results from finite-fault inversion. Based on this analysis, we estimated a rupture velocity of 3.25 km/s as the best fit, which is approximately 20% higher than the velocity estimated from the finite-fault analysis of 2.7 km/s. Unlike other events with a preferred near-vertical fault plane, determination of rupture velocity did not reach a stable minimum. This event shows good convergence of the misfit minimum for the preferred fault plane NP2, indicating a faster rupture velocity than that determined from the finite-fault analysis. The rupture velocity obtained from the directivity analysis is 72% of the average shear wave velocity at the corresponding depth.

4.5. The 25 January 2014 M_W 6.1 Java earthquake

The M_W 6.1 earthquake occurred in Kebumen, southern Java, at 05:14:18 UTC on 25 January 2014. The epicenter location from the USGS was 7.986°S and 109.265°E, with a focal depth of 66 km. Preliminary tests of the focal mechanism (strike ϕ and dip δ) were conducted (Fig. S17) and defined the two nodal planes with a rectangular fault plane with dimensions of 24 km along strike and 26 km down-dip. The fault plane was divided into 156 subfaults with a grid size of 2.0 km × 2.0 km. We used 35 teleseismic stations, including 23 P-wave, 8 SH-wave, 27 Rayleigh-wave, and 5 Love-wave seismograms (Fig. 6a and 6b). The displacement waveforms for each body wave had a length of 15 s from the P-wave first arrival, and the long-period surface waves were analyzed up to 3600 s from the origin time. For the 2014 event, the optimal solution obtained for strike, dip, and rake for the two nodal planes was NP1 ($\phi = 114^o, \delta = 76^o, \lambda = -88^o$) and NP2 ($\phi = 284^o, \delta = 14^o, \lambda = -97^o$) (Table 1).

The synthetic waveforms (Figs. S18 and S19) demonstrate good agreement with the observed waveforms with a minimum cumulative misfit of 0.252 for NP2 as the subhorizontal fault plane. Fig. 6c and 6d show the STF and slip distribution of NP2, respectively, exhibiting a simple rupture process with a total duration of approximately 6 s. The rupture was initiated from a depth of 66 km with a maximum slip of 43.2 cm. The corresponding rupture length from the finite-fault analysis was $L = 12$ km. The average slip of this event was approximately 18.6 cm. The slip vectors depicted mainly a normal faulting mechanism, dominated by circular rupture propagation with an average rupture velocity of about 2.9 km/s along the down-dip direction. The total seismic moment for NP2 was 1.96×10^{18} Nm, which is equivalent to an M_W 6.1 earthquake based on Hanks and Kanamori (1979). The moment magnitude calculated using the seismic moment of the earthquake was similar to the moment magnitude reported in the GCMT solution. Using the fault area (A) with total dimensions from the subfaults with slip larger than 10% of the maximum slip (Fig. 6d), the static stress drop ($\Delta\sigma_s$) was approximately 1.7 MPa. Fig. 6e shows the map view of this slip distribution of the subhorizontal fault plane, which resulted in damage to the cities of Kebumen, Banyumas, and Cilacap in Central Java.

Fig. 6f shows the fitting curves between the observed ASTFs and the calculated Δt for NP1 and NP2 after testing various rupture velocities in the directivity analysis. This shows that the subhorizontal fault plane (NP2) is a preferred fault plane as it shows an L1-misfit of 1.02 compared with that of the near-vertical fault plane (NP1) of 1.08 (Fig. S20), confirming the results of the finite-fault inversion analysis. This subhorizontal fault plane aligns with the report by Serhalawan et al. (2017) using the distribution of relocated aftershocks. From this, we estimated a rupture velocity of 2.25 km/s as the best solution, which is approximately 20% slower than the velocity from the finite-fault analysis of 2.9 km/s. This rupture velocity is only approximately 60% of the shear wave velocity at the corresponding depth.

5. Discussion

With the exception of the 1998 event, the analyzed earthquakes predominantly showed simple rupture behavior. Most of the events had a triangular-shaped STF (Fig. 2c-6c), with a single and compact asperity (Fig. 2d-6d). Except for the 2014 event, the slip distributions primarily exhibited a unilateral down-dip rupture (Fig. 2d-6d), which aligns with findings from previous studies on intermediate-depth earthquakes (Shiddiqi et al., 2018; Twardzik and Ji, 2015). The STF of the 1998 event displayed a double-peak, suggesting the moment was released from two subevents. Our obtained STF results were mostly comparable with those of the 2014 Rat Islands intermediate-depth earthquake (Twardzik and Ji, 2015; Ye et al., 2014), which also exhibited a similar single triangle shape. In contrast, the STF of the 2019 Peru earthquake showed three-peaked pulses (Liu and Yao, 2020; Ye et al., 2020). It is important to note that the rupture behavior and characteristics of intermediate-depth earthquakes along the Java subduction zone remain poorly understood, despite they can be very damaging. Further investigations would be necessary to determine if there is a relationship between this simple rupture behavior and regional tectonic settings along this subduction zone.

The estimated rupture sizes (lengths and widths, Table 1) are comparable with those of other moderate-magnitude shallow earthquakes in Sumbawa, Indonesia (Sianipar et al., 2022). Sianipar et al. (2022) employed the autocorrelation function of slip along the strike and dip directions following Mai and Beroza (2000) to obtain the effective rupture dimensions and compared these results with the removal of subfaults with slip amplitudes smaller than 17% of the maximum slip as suggested by Ye et al. (2016).

Ye et al. (2016) indicated an average stress drop of 3.0–4.0 MPa based on the energy-related global finite-fault model. In our analysis, we estimated static stress drop ($\Delta\sigma_s$) ranging from approximately 1.7 MPa to 3.0 MPa, while lower values of 0.8 MPa and 0.9 MPa for the 1998 and 2001 earthquakes, respectively (Table 1). While stress drop estimation contains uncertainties, our results fall within the range observed for shallow earthquakes (1 −10 MPa; Tibi et al., 2002) and are similar to the stress drop observed for the 2018 Anchorage, Alaska, intraslab earthquake ($\Delta\sigma = 2.76$ MPa; Liu et al., 2019). Twardzik and Ji (2015) estimated a static stress drop of 3.8 MPa to 6.2 MPa for a steeply dipping fault plane. Moreover, Ye et al. (2020) suggested a slip-weighted average stress drop of 5.2 MPa and an area-based stress drop of 2.3 MPa. However, our estimated stress drops are lower than results observed in some other intermediate-depth earthquakes, for example, the Vrancea earthquake ($\Delta\sigma =$ 10 MPa; Gusev et al., 2002), Rat Islands earthquake ($\Delta\sigma = 11.8$ MPa; Ye et al., 2014), and Tarapaca earthquake ($\Delta\sigma = 33$ MPa; Kuge et al., 2010). Warren (2014) proposed that earthquakes which result in new faults tend to have higher stress drops and lower seismic efficiency than reactivated faults. The relatively low stress drop in the southern Java subduction zone might be indicative of frequent seismic activity. This subduction zone is also marked by an absence of significant megathrust earthquakes with $M_W \geq 8$ (Newcomb and McCann, 1987; Okal, 2012), suggesting that there is a lack of large asperities. In addition, a tomography study revealed the presence of fluid in the upper crust beneath the center of Java Island, particularly in sedimentary basins and around volcanic centers (Bohm et al., 2013). This study also found the presence of fluid above the subducting slab in the marine forearc and in the mantle wedge beneath the volcanic arc.

Goldberg et al. (2022) provided evidence that teleseismic data can be used effectively to estimate moment release, even when the detailed rupture behavior is not well characterized. However, it is important to recognize the limitations of our teleseismic-only inversion results in terms of spatial resolution. These limitations can introduce uncertainties when estimating the average static stress drop (Adams et al., 2017), despite our efforts to focus on subfaults with better-constrained slips.

The average rupture velocity obtained from finite-fault inversion for the events in our study ranged from approximately 2.6 km/s to 2.9 km/s along the down-dip propagation direction (Table 1). This rupture velocity is comparable with findings from other studies on intermediate-depth earthquakes. For instance, Liu and Yao (2020) reported a rupture velocity of ~2.7 km/s, and Ye et al. (2020) found a velocity of ~3 km/s for the 2019 Peru earthquake, while Twardzik and Ji (2015) observed a velocity of ~2 km/s for the 2014 Rat Islands earthquake. In our study, we obtained similar rupture velocities through both finite-fault inversion and directivity analysis for three events (1999, 2001, and 2014, Table 1). However, we encountered significant differences in the estimated rupture velocity for the 1998 and 2017 events, likely due to data limitations and distribution of stations when conducting directivity analysis. The teleseismic stations are primarily located in azimuth to the north direction, with fewer stations available in the south–southwest direction. It is rather crucial for ruptured fault plane and velocity determination for two fault planes that are nearly vertical and subhorizontal. Although estimating rupture velocity using directivity analysis is challenging due to limited data and station coverage for earthquakes with steep and subhorizontal fault planes, the rupture velocities derived from the directivity analysis showed variation of approximately ±10% to 20% compared with those from finite-fault inversion, except for the 1998 and 2017 events, as listed in Table 1. For these intermediate-depth earthquakes, the shear wave velocity near the epicenter was approximately 4.5 km/s, and the rupture velocities determined in this study ranged from 0.5 to 0.9 times the shear wave velocity. Despite the inherent uncertainty and challenges in definitively determining rupture velocity using teleseismic records, it shows a tendency that events which preferred near-vertical fault planes generally exhibited higher rupture velocities compared with events which preferred subhorizontal rupture planes. For instance, Ye et al. (2017) suggested a steeply dipping fault plane with a high rupture velocity of 3.5 km/s for the 2017 Chiapas, Mexico, earthquake. On the other hand, Ye et al. (2014) indicated a shallow-dipping rupture plane with a low rupture velocity of about 1.5 km/s for the 2014 Rat Islands earthquake.

Previous studies have employed uncertainty analysis techniques, such as jackknife and bootstrap methods (Asano and Iwata, 2009; Hayes, 2011; Sianipar et al., 2022), to investigate the stability and accuracy of finite-fault inversion results by resampling the original data set with or without replacement. In our study, we accounted for uncertainties by conducting a series of initial finite-fault inversions and reviewing the results. This involved removing poor-quality stations, manual adjustment of waveform picking in time, and visual adjustment of fault plane size (Figs. S21-S25). We also allowed the rupture velocity and rake angle to vary within a certain range from the reference values, and we conducted preliminary inversion tests on the strike and dip values obtained from the GCMT solution to verify the fault geometry (Figs. S1, S5, S9, S13, and S17).

Although there were insufficient seismic stations in the south–southwest direction, the directivity analysis provided valuable constraints for determining the rupture plane. The results indicate that three events had preferred rupture planes with near-vertical fault planes with the strike parallel to the trench direction, and two events had subhorizontal fault planes with strikes parallel and perpendicular to the trench direction. The preferred fault planes determined from this analysis are also depicted in Fig. 1 alongside the focal mechanisms. Given the challenges in determining the rupture plane associated with the subducting slab, current deployment of more densely distributed national seismic networks in the Java region of Indonesia will provide important insights for understanding the dynamics of the subduction zone and its yielding seismic hazard assessments.

Previous studies on intermediate-depth earthquakes have shown a preference for near-vertical dipping fault planes. Tibi et al. (2002) suggested a near-vertical fault plane for the 14 October 1997 Fiji-Tonga earthquake (M_W 7.7, depth 167 km). Similarly, Twardzik and Ji (2015) identified a steeply-dipping fault plane based on the distribution of relocated aftershocks for the 2014 Rat Islands earthquake. Liu and Yao (2020) and Ye et al. (2020) also favored an eastward-dipping nodal

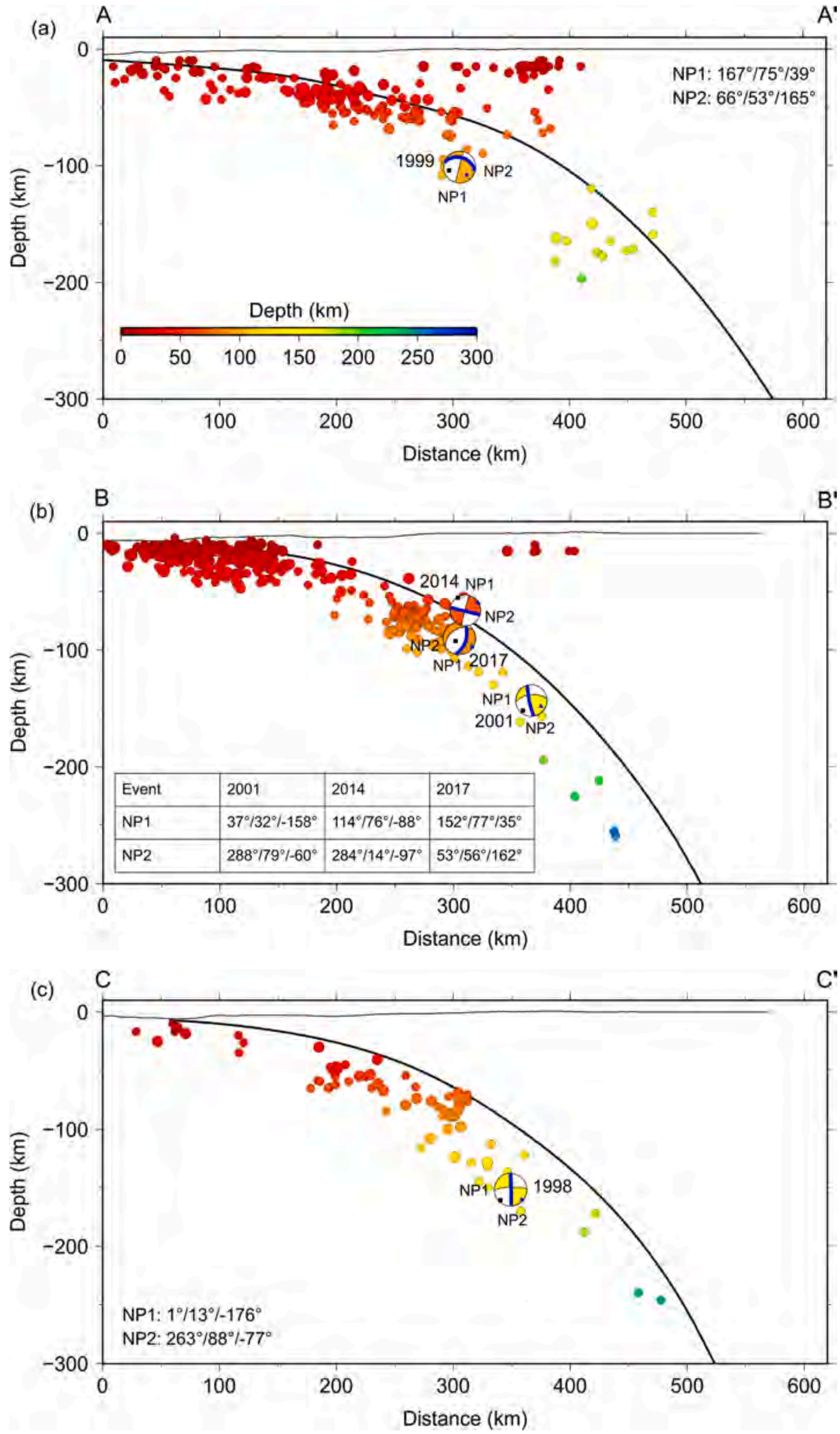

Event	2001	2014	2017
NP1	37°/32°/-158°	114°/76°/-88°	152°/77°/35°
NP2	288°/79°/-60°	284°/14°/-97°	53°/56°/162°

Fig. 7. Side projections along the AA', BB', and CC' profiles in Fig. 1 with background seismicity for earthquakes: (a) 1999 Southern Sumatra along AA'; (b) 2017 Java, 2014 Java, and 2001 Java along BB'; and (c) 1998 Java along CC'. The beachballs show the optimal focal mechanism solutions from our preliminary inversion tests. The thick blue lines on each beachball indicate the preferred fault planes identified from directivity analysis, whereas black squares and blue triangles represent the orientation of the P- and T-axes, respectively. Background seismicity is the same as in Fig. 1. The color scale in (a) indicates the depth of events and background seismicity. The solid black lines denote the Slab2.0 model (Hayes et al., 2018). (For interpretation of the references to color in this figure legend, the reader is referred to the web version of this article.)

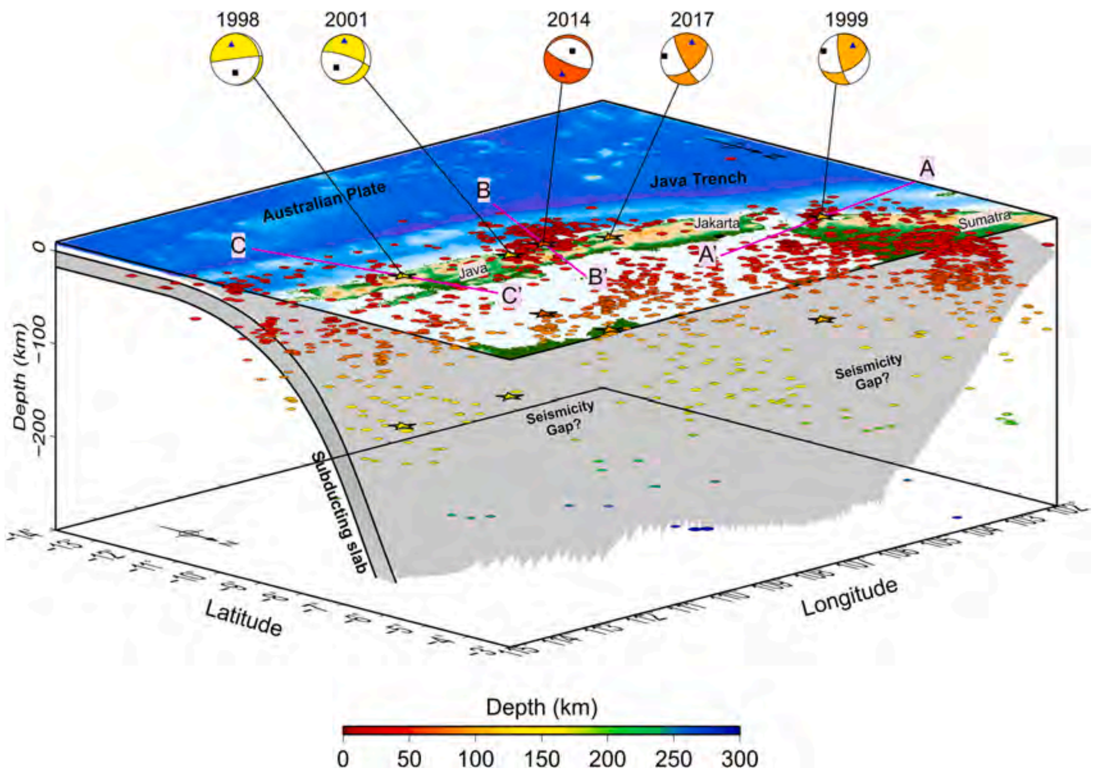

Fig. 8. Perspective view of the 3D seismicity distribution of the study area, looking at the Java Trench from the northeast–southwest direction. The stars show the epicenters and hypocenters of the five analyzed events with their focal mechanism solutions. Black squares and blue triangles on each beachball represent the orientation of the P- and T-axes, respectively. The light gray color represents the subducting slab extracted from Slab2.0 (Hayes et al., 2018). (For interpretation of the references to color in this figure legend, the reader is referred to the web version of this article.)

plane (NP1; strike 353° and dip 57°) with a higher dip than NP2 (strike 162° and dip 33°) for the 2019 Peru earthquake. On the other hand, other studies have found predominantly subhorizontal fault planes. Warren et al. (2007, 2008) and Warren (2014) conducted directivity analysis of intermediate-depth earthquakes using teleseismic records and observed primarily subhorizontal fault planes, with some near-vertical fault planes, in subduction zones such as those in the Tonga-Kermadec region, Central America, and South America. Ye et al. (2014), in contrast to Twardzik and Ji (2015), suggested a shallow-dipping fault plane for the 2014 Rat Islands earthquake based on the horizontal distribution of aftershocks and back-projection results. Additionally, Kiser et al. (2011) identified predominantly subhorizontal fault planes in several subduction zones using the back-projection technique applied to 22 intermediate-depth events. These findings highlight the challenges in definitively determining the ruptured fault plane for intermediate-depth earthquakes.

The physical mechanism of intermediate-depth earthquakes is still a subject of debate, with one prominent hypothesis relating to dehydration within subducting plates. Dehydration embrittlement is commonly used to explain the occurrence of intermediate-depth earthquakes (Hacker et al., 2003; Okazaki and Hirth, 2016). This mechanism involves an increase in pore pressure caused by dehydration, which compensates for the overburden pressure and leads to brittle failure (Zhan, 2020). This can result in reactivation of pre-existing faults or the creation of new faults. In our directivity analysis, we found three events with near-vertical fault planes and two events with subhorizontal fault planes as our solutions. Warren et al. (2008) suggested that subhorizontal fault planes are associated with the creation of new faults, while subvertical fault planes are linked to the reactivation of outer rise faults. Reactivation of pre-existing faults as a mechanism for generating intermediate-depth earthquakes has been proposed in several subduction zones (Kiser et al., 2011; Ranero et al., 2003, 2005; Yamasaki and Seno, 2003). Marot et al. (2012) proposed that reactivated pre-existing faults may be controlled by slab bending or unbending stress. Although the specific generating mechanism for our target events remains unclear, we support the hypothesis suggesting the reactivation of pre-existing faults or the creation of new faults in the slab due to dehydration embrittlement.

As shown in Fig. 1, the T-axes of our analyzed earthquakes are generally consistent in the north–south to northeast–southwest orientations with intermediate plunges. To analyze the stress patterns of intermediate-depth earthquakes in the Java subduction zone, we projected the P- and T-axes of the five analyzed events and the background of intermediate-depth events (Fig. S26a) into two reference frame projection systems, geographic and regional frames, following a technique used by Chen et al. (2001, 2004) (Fig. S26b). The geographic frame comprises the north, east, and down (N-E-D) coordinate system, while the regional frame is in the slab reference system with the along-strike, slab-normal, and down-dip (AS-SN-DD) coordinate system. Using the seismicity distribution in this region, we determined the slab geometry (strike and dip) employing a linear fitting method (Chen et al., 2001, 2004). Based on this technique, we obtained the slab geometry of Java with a strike of 299° and dip of 56°, subducting in the northeast direction. The results revealed that in the geographic frame, the T-axes are predominantly oriented in the northeast azimuth (0° to 60°), with a plunge ranging from 30° to 82° (Fig. S26b, left). This primarily northeast clustering of T-azimuths not only suggests its dominance but also is consistent with the Australian Plate's northeastward subduction. In the regional frame, the T-axes are predominantly distributed around the center of the projection, suggesting a predominantly down-dip extension (Fig. S26b, right). However, the shallowest earthquake (depth 66 km) is an exception, exhibiting a down-dip compressive stress (Fig. S26).

We took three profiles (AA', BB', and CC') mostly perpendicular to the preferred fault planes from the epicenter (Fig. 1). We included side projections of their focal mechanisms along with background seismicity for each earthquake, as shown in Fig. 7a-7c. The events of 2001, 2014, and 2017 were placed in the same profile of BB'. For the 1999 and 2014 events, the preferred fault planes appear to be parallel to the bending of the slab. In contrast, the preferred fault planes for the other events are near-vertical dipping planes beneath the slope of the slab. Notably, a previous study identified seismic gaps at depths of less than 50 km in the south of Java, which poses a potential risk for future megathrust earthquakes (Widiyantoro et al., 2020). In our study, we also observed seismicity gaps at depths ranging from approximately 100 km to 200 km. To support this interpretation, we made a perspective view of the three-dimensional (3D) seismicity distribution of the study area in the Java subduction zone, as shown in Fig. 8. These gaps could potentially be associated with larger earthquakes in future with M_W>7. Therefore, this densely populated region requires closer attention as the occurrence and distribution of intermediate-depth earthquakes are difficult to predict due to their infrequency and the lack of historical records.

6. Conclusion

In this study, we focused on investigating the finite-fault rupture models and deriving source time functions (STFs) for five intermediate-depth earthquakes that occurred between 1998 and 2017 with magnitudes (M_W) greater than 6.1 in the southern region of Java and its surrounding areas. Our finite-fault inversions were constrained by teleseismic body waves and surface waves. Overall, our analysis revealed that the rupture process of the investigated events was relatively simple, with the exception of the 1998 event. The rupture processes were indicated by a triangular STF with a singular and compact asperity, while the slip distribution mainly exhibited unilateral down-dip rupture, except for the 2014 event. In addition to the finite-fault inversions, we conducted directivity analysis to validate the preferred fault planes of the target events. The results suggest that three events exhibited near-vertical fault planes (in the down-dip direction) along a strike parallel to the trench direction, while two events displayed sub-horizontal fault planes along a strike perpendicular and parallel to the trench direction (down-dip and circular direction). The estimated static stress drops revealed comparable values to those obtained for intermediate-depth earthquakes in other subduction zones. The source characteristics and rupture models obtained through our study offer valuable insights for seismic hazard assessments in the densely populated region of Java Island, Indonesia. By understanding the behavior of these intermediate-depth earthquakes, we can better assess and mitigate potential risks in the area.

Funding

This research was funded by the Ministry of Science and Technology in Taiwan under grant MOST 110–2116-M−001−023−MY3.

CRediT authorship contribution statement

M. Megawati: Data curation, Formal analysis, Methodology, Visualization, Writing – original draft. **Kuo-Fong Ma:** Methodology, Project administration, Supervision, Validation, Writing – review & editing. **Po-Fei Chen:** Supervision, Validation. **Dimas Sianipar:** Data curation, Methodology, Validation. **Ming-Che Hsieh:** Methodology, Software.

Declaration of competing interest

The authors declare that they have no known competing financial interests or personal relationships that could have appeared to influence the work reported in this paper.

Data availability

I have shared the link to my data at the Attached File step

Acknowledgements

The teleseismic waveform data were retrieved from the Incorporated Research Institutions for Seismology (IRIS) Global Seismographic Network. The background seismicity and the focal mechanisms were retrieved from the International Seismological Center (ISC) and the Global Centroid Moment Tensor (GCMT), respectively. The authors thank Prof. Chen Ji (U.C. Santa Barbara) for the finite-fault inversion code. We thank the Agency for Meteorology, Climatology, and Geophysics of the Republic of Indonesia (BMKG) for providing a catalog of damaging earthquakes in Indonesia. We thank Prof. Walter Mooney for the valuable discussions and suggestions. We thank Yopi Serhalawan for helping with the projection of the P- and T-axes. We thank Hasbi Ash Shiddiqi for the discussions regarding the directivity analysis. The authors thank the editor and the reviewers for their constructive comments and suggestions to improve the quality of this paper. The figures were drawn using the Generic Mapping Tools (GMT) software package (Wessel and Smith, 1991). This research was funded by the Ministry of Science and Technology in Taiwan under grant MOST 110-2116-M-001-023-MY3. This work is financially supported by the Earthquake Disaster & Risk Evaluation and Management Center (E-DREaM) from the Featured Areas Research Center Program within the framework of the Higher Education Sprout Project by the Ministry of Education (MOE) in Taiwan. This publication is with the Taiwan Earthquake Center (TEC) under the Contribution Number 00188.

Appendix A. Supplementary material

Supplementary data to this article can be found online at https://doi.org/10.1016/j.jseaes.2024.106040.

References

Adams, M., Twardzik, C., Ji, C., 2017. Exploring the uncertainty range of coseismic stress drop estimations of large earthquakes using finite fault inversions. Geophys. J. Int. 208, 86–100.
Asano, K., Iwata, T., 2009. Source Rupture Process of the 2004 Chuetsu, Mid-Niigata Prefecture, Japan, Earthquake Inferred from Waveform Inversion with Dense Strong-Motion Data. Bull. Seismol. Soc. Am. 99, 123–140.
Astiz, L., Lay, T., Kanamori, H., 1988. Large intermediate-depth earthquakes and the subduction process. Phys. Earth Planet. In. 53, 80–166.
Bassin, C., Laske, G., Masters, G., 2000. The current limits of resolution for surface wave tomography in North America. EOS Trans AGU 81, F897.
Ben-Menahem, A., Singh, S.J., 1981. Representation of Seismic Sources. In: Ben-Menahem, A., Singh, S.J. (Eds.), Seismic Waves and Sources. Springer, New York, NY, pp. 151–256.
Bohm, M., Haberland, C., Asch, G., 2013. Imaging fluid-related subduction processes beneath Central Java (Indonesia) using seismic attenuation tomography. Tectonophysics 590, 175–188.
Cesca, S., Heimann, S., Dahm, T., 2011. Rapid directivity detection by azimuthal amplitude spectra inversion. J. Seismol. 15, 147–164.
Chen, P.-F., Bina, C.R., Okal, E.A., 2004. A global survey of stress orientations in subducting slabs as revealed by intermediate-depth earthquakes. Geophys. J. Int. 159, 721–733.
Chen, P.-F., Bina, C.R., Okal, E.A., 2001. Variations in slab dip along the subducting Nazca Plate, as related to stress patterns and moment release of intermediate-depth seismicity and to surface volcanism. Geochem. Geophys. Geosyst. 2.
Dębski, W., 2008. Estimating the Earthquake Source Time Function by Markov Chain Monte Carlo Sampling. Pure Appl. Geophys. 165, 1263–1287.
Dziewonski, A.M., Anderson, D.L., 1981. Preliminary reference Earth model. Phys. Earth Planet. In. 25, 297–356.
Ekström, G., Nettles, M., Dziewoński, A.M., 2012. The GCMT project 2004–2010: Centroid-moment tensors for 13,017 earthquakes. Phys. Earth Planet. In. 200–201, 1–9.
Engdahl, E.R., Di Giacomo, D., Sakarya, B., Gkarlaouni, C.G., Harris, J., Storchak, D.A., 2020. ISC-EHB 1964–2016, an Improved Data Set for Studies of Earth Structure and Global Seismicity. Earth and Space. Science 7.
Ferrand, T.P., Hilairet, N., Incel, S., Deldicque, D., Labrousse, L., Gasc, J., Renner, J., Wang, Y., Green II, H.W., Schubnel, A., 2017. Dehydration-driven stress transfer triggers intermediate-depth earthquakes. Nat. Commun. 8, 15247.
Fujita, K., Kanamori, H., 1981. Double seismic zones and stresses of intermediate depth earthquakes. Geophys. J. Int. 66, 131–156.
Futterman, W.I., 1962. Dispersive body waves. J. Geophys. Res. 1896–1977 (67), 5279–5291.
Gilbert, F., Dziewonski, A.M., Bullard, E.C., 1975. An application of normal mode theory to the retrieval of structural parameters and source mechanisms from seismic

spectra. Philosophical Transactions of the Royal Society of London. Series a, Mathematical and Physical Sciences 278, 187–269.

Goldberg, D.E., Koch, P., Melgar, D., Riquelme, S., Yeck, W.L., 2022. Beyond the Teleseism: Introducing Regional Seismic and Geodetic Data into Routine USGS Finite-Fault Modeling. Seismol. Res. Lett. 93, 3308–3323.

Goldstein, P., Snoke, A., 2005. SAC Availability for the IRIS Community. Incorporated Research Institutions for Seismology Newsletter 7.

Gunawan, E., Widiyantoro, S., Marliyani, G.I., Sunarti, E., Ida, R., Gusman, A.R., 2019. Fault source of the 2 September 2009 Mw 6.8 Tasikmalaya intraslab earthquake, Indonesia: Analysis from GPS data inversion, tsunami height simulation, and stress transfer. Phys. Earth Planet. In. 291, 54–61.

Gusev, A., Radulian, M., Rizescu, M., Panza, G.F., 2002. Source scaling of intermediate-depth Vrancea earthquakes. Geophys. J. Int. 151, 879–889.

Hacker, B.R., Peacock, S.M., Abers, G.A., Holloway, S.D., 2003. Subduction factory 2. Are intermediate-depth earthquakes in subducting slabs linked to metamorphic dehydration reactions? Journal of Geophysical Research: Solid. Earth 108.

Hall, R., Spakman, W., 2015. Mantle structure and tectonic history of SE Asia. Tectonophysics 658, 14–45.

Hanks, T.C., Kanamori, H., 1979. A moment magnitude scale. J. Geophys. Res. Solid Earth 84, 2348–2350.

Hao, J., Ji, C., Wang, W., Yao, Z., 2013. Rupture history of the 2013 Mw 6.6 Lushan earthquake constrained with local strong motion and teleseismic body and surface waves. Geophys. Res. Lett. 40, 5371–5376.

Hao, J., Ji, C., Yao, Z., 2017. Slip history of the 2016 Mw 7.0 Kumamoto earthquake: Intraplate rupture in complex tectonic environment. Geophys. Res. Lett. 44, 743–750.

Hayes, G.P., 2011. Rapid source characterization of the 2011 Mw 9.0 off the Pacific coast of Tohoku Earthquake. Earth Planets Space 63, 529–534.

Hayes, G.P., Moore, G.L., Portner, D.E., Hearne, M., Flamme, H., Furtney, M., Smoczyk, G.M., 2018. Slab2, a comprehensive subduction zone geometry model. Science 362, 58–61.

Helmberger, D.V., 1983. Theory and application of synthetic seismograms. In: Kanamori, H., Boschi, E. (Eds.), Earthquakes: Observation Theory and Interpretation. North-Holland Publishing Company, pp. 174–222.

Hsieh, M., Zhao, L., Ji, C., Ma, K., 2016. Efficient Inversions for Earthquake Slip Distributions in 3D Structures. Seismol. Res. Lett. 87, 1342–1354.

Irsyam M., Widiyantoro S., Natawidjaja D.H., Meilano I., Rudyanto A., Hidayati S., Triyoso W., Hanifa N.R., Djarwadi D., & Faizal L. (editor) & Sunarjito National Team for updating of Indonesia Earthquake Hazard Map 2017., 2017. Earthquake Source and Hazard Map of Indonesia 2017. Indonesia National Center for Earthquake Studies, Research and Development Agency of Ministry of Public Work and Housing, Indonesia.

Isacks, B., Molnar, P., 1971. Distribution of stresses in the descending lithosphere from a global survey of focal-mechanism solutions of mantle earthquakes. Rev. Geophys. 9, 103–174.

Ji, C., Wald, D.J., Helmberger, D.V., 2002. Source Description of the 1999 Hector Mine, California, Earthquake, Part I: Wavelet Domain Inversion Theory and Resolution Analysis. Bull. Seismol. Soc. Am. 92, 1192–1207.

Ji, C., Helmberger, D.V., Wald, D.J., Ma, K.-F., 2003. Slip history and dynamic implications of the 1999 Chi-Chi, Taiwan, earthquake. Journal of Geophysical Research: Solid. Earth 108.

Jung, H., Green II, H.W., Dobrzhinetskaya, L.F., 2004. Intermediate-depth earthquake faulting by dehydration embrittlement with negative volume change. Nature 428, 545–549.

Kanamori, H., Anderson, D.L., 1975. Theoretical basis of some empirical relations in seismology. Bull. Seismol. Soc. Am. 65, 1073–1095.

Kelemen, P.B., Hirth, G., 2007. A periodic shear-heating mechanism for intermediate-depth earthquakes in the mantle. Nature 446, 787–790.

Kennett, B.L.N., Engdahl, E.R., 1991. Traveltimes for global earthquake location and phase identification. Geophys. J. Int. 105, 429–465.

Kirby, S.H., Stein, S., Okal, E.A., Rubie, D.C., 1996. Metastable mantle phase transformations and deep earthquakes in subducting oceanic lithosphere. Rev. Geophys. 34, 261–306.

Kiser, E., Ishii, M., Langmuir, C.H., Shearer, P.M., Hirose, H., 2011. Insights into the mechanism of intermediate-depth earthquakes from source properties as imaged by back projection of multiple seismic phases. Journal of Geophysical Research: Solid. Earth 116.

Kopp, H., Flueh, E.R., Petersen, C.J., Weinrebe, W., Wittwer, A., Scientists, M., 2006. The Java margin revisited: Evidence for subduction erosion off Java. Earth Planet. Sci. Lett. 242, 130–142.

Koulali, A., McClusky, S., Susilo, S., Leonard, Y., Cummins, P., Tregoning, P., Meilano, I., Efendi, J., Wijanarto, A.B., 2017. The kinematics of crustal deformation in Java from GPS observations: Implications for fault slip partitioning. Earth Planet. Sci. Lett. 458, 69–79.

Kuge, K., Kase, Y., Urata, Y., Campos, J., Perez, A., 2010. Rupture characteristics of the 2005 Tarapaca, northern Chile, intermediate-depth earthquake: Evidence for heterogeneous fluid distribution across the subducting oceanic plate? Journal of Geophysical Research: Solid. Earth 115.

Langston, C.A., Helmberger, D.V., 1975. A Procedure for Modelling Shallow Dislocation Sources*. Geophys. J. Int. 42, 117–130.

Lin, X., Chu, R., Zeng, X., 2019. Rupture processes and Coulomb stress changes of the 2017 Mw 6.5 Jiuzhaigou and 2013 Mw 6.6 Lushan earthquakes. Earth Planets Space 71, 1–15.

Liu, C., Lay, T., Xie, Z., Xiong, X., 2019. Intraslab Deformation in the 30 November 2018 Anchorage, Alaska, MW 7.1 Earthquake. Geophys. Res. Lett. 46, 2449–2457.

Liu, W., Yao, H., 2020. Rupture Process of the 26 May 2019 Mw 8.0 Northern Peru Intermediate-Depth Earthquake and Insights Into Its Mechanism. Geophys. Res. Lett. 47.

Liu, L., Zhang, J.S., 2015. Differential contraction of subducted lithosphere layers generates deep earthquakes. Earth Planet. Sci. Lett. 421, 98–106.

López-Comino, J.Á., Stich, D., Ferreira, A.M.G., Morales, J., 2015. Extended fault inversion with random slipmaps: a resolution test for the 2012 Mw 7.6 Nicoya. Costa Rica Earthquake. Geophysical Journal International 202, 1505–1521.

Mai, P.M., Beroza, G.C., 2000. Source Scaling Properties from Finite-Fault-Rupture Models. Bull. Seismol. Soc. Am. 90, 604–615.

Marot, M., Monfret, T., Pardo, M., Ranalli, G., Nolet, G., 2012. An intermediate-depth tensional earthquake (MW 5.7) and its aftershocks within the Nazca slab, central Chile: A reactivated outer rise fault? Earth Planet. Sci. Lett. 327–328, 9–16.

Masson, D.G., Parson, L.M., Milsom, J., Nichols, G., Sikumbang, N., Dwiyanto, B., Kallagher, H., 1990. Subduction of seamounts at the Java Trench: a view with long-range sidescan sonar. Tectonophysics 185, 51–65.

Mori, J., Mooney, W.D., Afnimar, Kurniawan, S., Anaya, A.I., Widiyantoro, S., 2007. The 17 July 2006 Tsunami Earthquake in West Java, Indonesia. Seismol. Res. Lett. 78, 201–207.

Nakajima, J., Uchida, N., Shiina, T., Hasegawa, A., Hacker, B.R., Kirby, S.H., 2013. Intermediate-depth earthquakes facilitated by eclogitization-related stresses. Geology 41, 659–662.

Newcomb, K.R., McCann, W.R., 1987. Seismic history and seismotectonics of the Sunda Arc. J. Geophys. Res. Solid Earth 92, 421–439.

Okal, E.A., 2012. The south of Java earthquake of 1921 September 11: a negative search for a large interplate thrust event at the Java Trench. Geophys. J. Int. 190, 1657–1672.

Okazaki, K., Hirth, G., 2016. Dehydration of lawsonite could directly trigger earthquakes in subducting oceanic crust. Nature 530, 81–84.

Prieto, G.A., 2022. The Multitaper Spectrum Analysis Package in Python. Seismol. Res. Lett. 93, 1922–1929.

Prieto, G.A., Parker, R.L., Vernon III, F.L., 2009. A Fortran 90 library for multitaper spectrum analysis. Comput. Geosci. 35, 1701–1710.

Prieto, G.A., Florez, M., Barrett, S.A., Beroza, G.C., Pedraza, P., Blanco, J.F., Poveda, E., 2013. Seismic evidence for thermal runaway during intermediate-depth earthquake rupture. Geophys. Res. Lett. 40, 6064–6068.

Ranero, C.R., Villaseñor, A., Phipps Morgan, J., Weinrebe, W., 2005. Relationship between bend-faulting at trenches and intermediate-depth seismicity. Geochemistry, Geophysics, Geosystems 6.

Ranero, C.R., Phipps Morgan, J., McIntosh, K., Reichert, C., 2003. Bending-related faulting and mantle serpentinization at the Middle America trench. Nature 425, 367–373.

Ryan, W.B.F., Carbotte, S.M., Coplan, J.O., O'Hara, S., Melkonian, A., Arko, R., Weissel, R.A., Ferrini, V., Goodwillie, A., Nitsche, F., Bonczkowski, J., Zemsky, R., 2009. Global Multi-Resolution Topography synthesis. Geochemistry, Geophysics, Geosystems 10.

Semmane, F., Benabdeloued, B.Y.N., Heddar, A., Khelif, M.F., 2017. The 2014 Mihoub earthquake (Mw4.3), northern Algeria: empirical Green's function analysis of the mainshock and the largest aftershock. J. Seismol. 21, 1385–1395.

Serhalawan, Y.R., Sianipar, D., Suardi, I., 2017. The January 25th, 2014 Kebumen earthquake: A normal faulting in subduction zone of Southern Java. AIP Conf. Proc. 1857, 030002.

Seton, M., Müller, R.D., Zahirovic, S., Williams, S., Wright, N.M., Cannon, J., Whittaker, J.M., Matthews, K.J., McGirr, R., 2020. A Global Data Set of Present-Day Oceanic Crustal Age and Seafloor Spreading Parameters. Geochem. Geophys. Geosyst. 21.

Shao, G., Li, X., Ji, C., Maeda, T., 2011. Focal mechanism and slip history of the 2011 Mw 9.1 off the Pacific coast of Tohoku Earthquake, constrained with teleseismic body and surface waves. Earth Planets Space 63, 559–564.

Shiddiqi, H.A., Tun, P.P., Kyaw, T.L., Ottemöller, L., 2018. Source Study of the 24 August 2016 Mw 6.8 Chauk, Myanmar. Earthquake. Seismological Research Letters 89, 1773–1785.

Sianipar, D., Huang, B.-S., Ma, K.-F., Hsieh, M.-C., Chen, P.-F., Daryono, D., 2022. Similarities in the rupture process and cascading asperities between neighboring fault patches and seismic implications: The 2002–2009 Sumbawa (Indonesia) earthquakes with moment magnitudes of 6.2–6.6. J. Asian Earth Sci. 229, 105167.

Simons, W.J.F., Socquet, A., Vigny, C., Ambrosius, B.a.C., Haji Abu, S., Promthong, C., Subarya, C., Sarsito, D.A., Matheussen, S., Morgan, P., Spakman, W., 2007. A decade of GPS in Southeast Asia: Resolving Sundaland motion and boundaries. Journal of Geophysical Research: Solid. Earth 112.

Sirait, A.M.M., Meltzer, A.S., Waldhauser, F., Stachnik, J.C., Daryono, D., Fatchurochman, I., Jatnika, J., Sembiring, A.S., 2020. Analysis of the 15 December 2017 Mw 6.5 and the 23 January 2018 Mw 5.9 Java Earthquakes. Bull. Seismol. Soc. Am. 110, 3050–3063.

Somerville, P., Irikura, K., Graves, R., Sawada, S., Wald, D., Abrahamson, N., Iwasaki, Y., Kagawa, T., Smith, N., Kowada, A., 1999. Characterizing Crustal Earthquake Slip Models for the Prediction of Strong Ground Motion. Seismol. Res. Lett. 70, 59–80.

Strasser, F.O., Arango, M.C., Bommer, J.J., 2010. Scaling of the Source Dimensions of Interface and Intraslab Subduction-zone Earthquakes with Moment Magnitude. Seismol. Res. Lett. 81, 941–950.

Tibi, R., Bock, G., Estabrook, C.H., 2002. Seismic body wave constraint on mechanisms of intermediate-depth earthquakes. Journal of Geophysical Research: Solid. Earth 107.

Tregoning, P., Brunner, F.K., Bock, Y., Puntodewo, S.S.O., McCaffrey, R., Genrich, J.F., Calais, E., Rais, J., Subarya, C., 1994. First geodetic measurement of convergence across the Java Trench. Geophys. Res. Lett. 21, 2135–2138.

Twardzik, C., Ji, C., 2015. The Mw 7.9 2014 intraplate intermediate-depth Rat Islands earthquake and its relation to regional tectonics. Earth Planet. Sci. Lett. 431, 26–35.
Viegas, G., 2012. Source Parameters of the 16 July 2010 Mw 3.4 Germantown, Maryland Earthquake. Seismol. Res. Lett. 83, 933–944.
Wang, K., Bilek, S.L., 2014. Invited review paper: Fault creep caused by subduction of rough seafloor relief. Tectonophysics 610, 1–24.
Warren, L.M., 2014. Dominant fault plane orientations of intermediate-depth earthquakes beneath South America. J. Geophys. Res. Solid Earth 119, 5762–5785.
Warren, L.M., Hughes, A.N., Silver, P.G., 2007. Earthquake mechanics and deformation in the Tonga-Kermadec subduction zone from fault plane orientations of intermediate- and deep-focus earthquakes. Journal of Geophysical Research: Solid. Earth 112.
Warren, L.M., Langstaff, M.A., Silver, P.G., 2008. Fault plane orientations of intermediate-depth earthquakes in the Middle America Trench. Journal of Geophysical Research: Solid. Earth 113.
Wessel, P., Smith, W.H.F., 1991. Free software helps map and display data. Eos Trans. AGU 72, 441–446.
Widiyantoro, S., Pesicek, J.D., Thurber, C.H., 2011. Subducting slab structure below the eastern Sunda arc inferred from non-linear seismic tomographic imaging. Geol. Soc. Lond. Spec. Publ. 355, 139–155.
Widiyantoro, S., Gunawan, E., Muhari, A., Rawlinson, N., Mori, J., Hanifa, N.R., Susilo, S., Supendi, P., Shiddiqi, H.A., Nugraha, A.D., Putra, H.E., 2020. Implications for megathrust earthquakes and tsunamis from seismic gaps south of Java Indonesia. Sci. Rep. 10, 15274.
Yamasaki, T., Seno, T., 2003. Double seismic zone and dehydration embrittlement of the subducting slab. Journal of Geophysical Research: Solid. Earth 108.
Ye, L., Lay, T., Kanamori, H., 2014. The 23 June 2014 Mw 7.9 Rat Islands archipelago, Alaska, intermediate depth earthquake. Geophys. Res. Lett. 41, 6389–6395.
Ye, L., Lay, T., Kanamori, H., Rivera, L., 2016. Rupture characteristics of major and great (Mw $\geq$ 7.0) megathrust earthquakes from 1990 to 2015: 1. Source parameter scaling relationships. J. Geophys. Res. Solid Earth 121, 826–844.
Ye, L., Lay, T., Bai, Y., Cheung, K.F., Kanamori, H., 2017. The 2017 Mw 8.2 Chiapas, Mexico, Earthquake: Energetic Slab Detachment. Geophysical Research Letters 44, 11824–11832.
Ye, L., Lay, T., Kanamori, H., 2020. Anomalously low aftershock productivity of the 2019 MW 8.0 energetic intermediate-depth faulting beneath Peru. Earth Planet. Sci. Lett. 549, 116528.
Yen, Y.-T., Ma, K.-F., 2011. Source-Scaling Relationship for M 4.6–8.9 Earthquakes, Specifically for Earthquakes in the Collision Zone of Taiwan. Bull. Seismol. Soc. Am. 101, 464–481.
Zhan, Z., 2020. Mechanisms and Implications of Deep Earthquakes. Annu. Rev. Earth Planet. Sci. 48, 147–174.
Zheng, X., Zhang, Y., Wang, R., Zhao, L., Li, W., Huang, Q., 2020. Automatic Inversions of Strong-Motion Records for Finite-Fault Models of Significant Earthquakes in and Around Japan. Journal of Geophysical Research: Solid. Earth 125.